RWTH-Aachen

Bachelor's Thesis in Physics

Sensitivity study of the MUSIC algorithm for LHC run 2

Yannik Kaiser

presented to

The Faculty of Mathematics, Computer Science and Natural Sciences
at RWTH Aachen University

III. Institute of Physics A

supervised by

Prof. Dr. Thomas Hebbeker

Aachen, 27th April 2021

Contents

1 Abstract

This thesis presents a study of the sensitivity of the Model Unspecific Search in CMS (MUSiC). The sensitivity study in MUSiC uses pseudo data sets of certain Beyond the Standard Model (BSM) theories generated corresponding to the conditions of proton-proton collisions at a centre of mass energy of $\sqrt{s} = 13$ TeV corresponding to an integrated luminosity of 137.0 fb^{-1}. The aim of this study is to determine the parameter space of the BSM models considered that the MUSiC analysis is sensitive to. The pseudo data of the BSM models and the simulation of the Standard Model (SM) background are analysed to study the ability of the MUSiC algorithm to identify deviations between a BSM signal and the SM background. Events are classified into hundreds of final states based on the final state objects in the events, with the requirement that at least one lepton is present in the final state, and kinematic distributions in each of the final states are examined. A following algorithm compares the signal and the simulation of the SM background to search for deviations. Compared to previously reported results, the impact of a luminosity increase from 35.9 fb^{-1} to 137.0 fb^{-1} on the limits of W′ and sphaleron signals is examined. The improved limits again demonstrate the capability of MUSiC and provide hope for significantly improved results from a subsequent full MUSiC analysis of future LHC data sets.

2 The Standard Model

2.1 Introduction

The Standard Model of elementary particle physics (SM) is, according to current knowledge, a very successful theory of particle physics [1, 2] whose predictions have been confirmed by many experiments. It contains knowledge about the elementary particles and their fundamental interactions. The Standard Model is designed to satisfy the laws of special relativity and quantum mechanics. The SM includes a description of the strong, weak and electromagnetic force leaving gravity as the only fundamental force that is not explained by the SM [3].
According to the SM, all the fundamental physics processes are described by 17 elementary particles and their interactions. The particles are classified into matter and exchange particles, while the interactions are divided into strong, weak and electromagnetic (Fig.2.1) [4, 5].

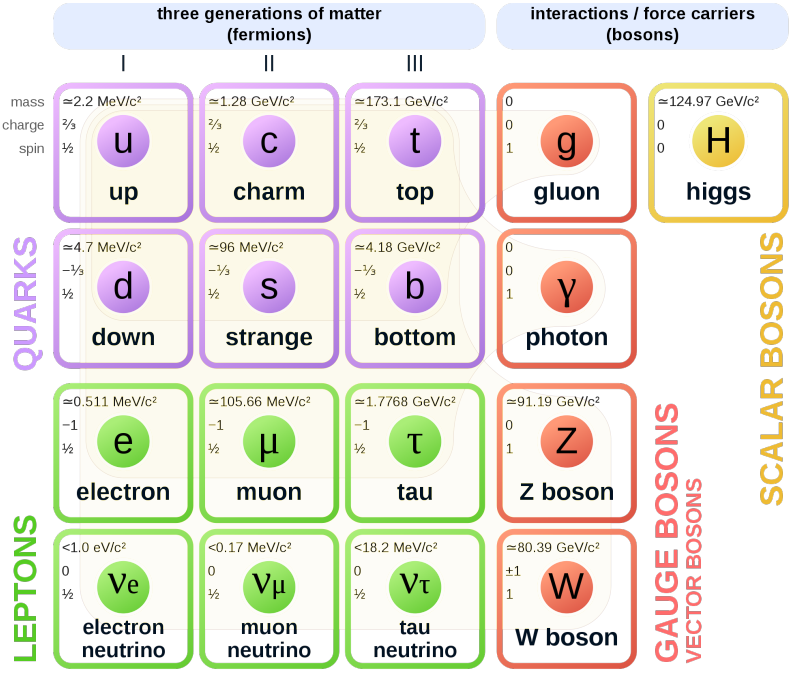

Fig. 2.1: Shown is the overview of the SM with the twelve fundermental fermions and the five fundermental bosons. The fermions are divided into quarks (purple) and leptons (green), which are differentiated into three generations. The bosons are divided into gauge/vector bosons (red) and scalar (yellow) bosons. The semi-transparent brown areas indicate which bosons can couple with which fermions (modified) [6].

2.2 Matter Particles

The category of matter particles includes 12 of the 17 particles, which are also called fermions due to their half-integer spin. Fermions are divided into quarks and leptons, which are differentiated into three generations. The matter particles of the second and third generation are heavier than those of the first; with the exception of neutrinos they are very unstable, which causes them to decay after a certain amount of time to particles of the first generation [2]. This also explains why the visible matter of our universe consists primarily of up and down quarks and electrons. Quarks are particles that form the atomic nuclei. Quarks can not be found freely in nature, they interact very quickly through the process of hadronisation to form hadrons, such as protons or neutrons etc. On the other hand leptons have a longer lifetime. The leptons exist both in charged form (e, μ, τ) and in neutral form (ν_e, ν_μ, ν_τ) [4]. The latter are the neutrinos, which interact very rarely and have such a small mass that it has not yet been possible to determine it precisely for all three.

2.3 Exchange particles & Interactions

In addition to matter particles, there are five other particles called bosons. They are divided into vector bosons (spin 1) and scalar (spin 0) bosons according to their spin. The vector bosons are associated with the fundamental forces, as they are the exchange particles that act as the carriers of the fundamental forces [7]. The Standard Model predicts three interactions, which will be explained in the following paragraphs (2.3.1 - 2.3.3).

2.3.1 Electromagnetic interaction

The electromagnetic interaction is characterised by the exchange of photons (γ). It is the interaction responsible for most common phenomena. Within this interaction, quarks as well as leptons e, μ and τ can participate by reacting with each other either through annihilation, radiation or absorption of a photon. The uncharged photon only couples with charged particles.

2.3.2 Strong interaction

The strong interaction is the interaction between quarks, which explains the cohesion of the hadrons. Moreover, the range of the strong interaction is limited to the size of the atomic nucleus (~10^{-15}m) [5]. The exchange particles of the strong interactions are the gluons (g). They can exchange a particular kind of charge called colour between fermions. Gluons carry different colour changes, that can be red, green, blue and their combinations. There are a total of eight different gluons considering their colour charges. Since gluons couple to particles with colour charges, they can even couple to themselves.

2.3.3 Weak interaction

In contrast to the strong interaction stands the weak interaction, which is not limited to the size of the atomic nucleus, but its strength decreases rapidly with increasing distance, which makes it perceptible up to a range of ~10^{-17}m [5]. Unlike the other interactions, the weak interaction has several bosons as exchange particles: the Z^0 boson and the $W^{\pm}$ bosons. The W bosons carry either a positive or negative charge, while the Z^0 boson is neutrally charged. In addition, the weak interaction can occur between all matter particles and is therefore the only interaction in which neutrinos can participate.

2.4 The Higgs Boson

One of the most challenging questions in particle physics is how to explain the mass of the fundamental particles. A possible explanation is given by the Higgs mechanism, a theory presented in 1964[1]. This theory asserts that the mass is provided to each particle through interaction with a new scalar boson, the Higgs boson, that is a particle associated with the hypothesised Brout-Englert-Higgs field. After several searches at particle collider based experiments, the Higgs boson was finally discovered by the CMS and ATLAS experiments in 2012 [11, 12]. The Higgs mechanism describes a field that is not equal to 0 in the ground state and whose coupling strength is proportional to the mass of the other particles (Fig.2.2) [5, 7]. The Higgs boson itself has a mass of 125.10±0.14 GeV [13] and is the only scalar boson discovered to date.

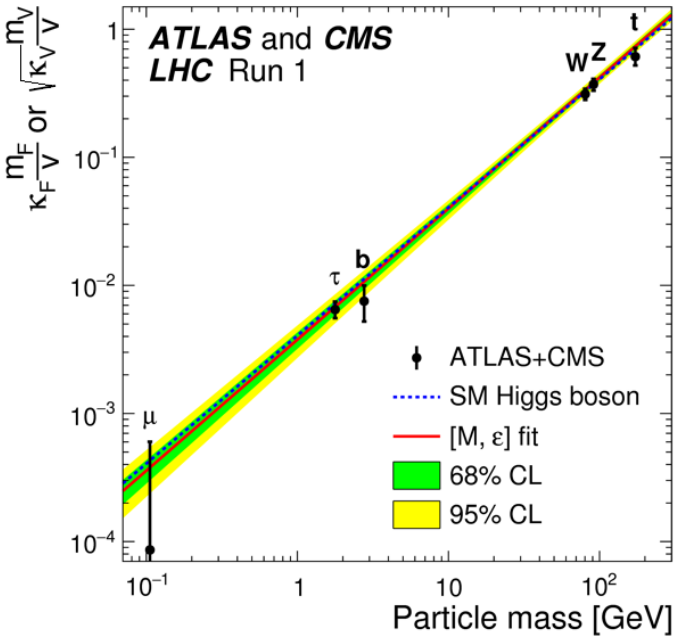

Fig. 2.2: Measurement results for the coupling of the Higgs boson to different particles. A deviation of the measurement from the expectation in the Standard Model (m_F/v or m_v/v for fermions and bosons, where v = 246 GeV is the vacuum expectation value of the Higgs field) is parameterised by the quantities κ_F or $\sqrt{\kappa_v}$, which are equal to one in the Standard Model (modified) [14].

[1] by Peter Higgs [8], François Englert, Robert Brout [9], T.W.B. Kibble, Carl R. Hagen and Gerald Guralnik [10]

2.5 Antiparticles

The SM predicts that for each particle there is an associated antiparticle, which has the same mass but, in the case of the leptons and quarks, for example, has the opposite charge. However, since they are only a different "form" of the elementary particles and are otherwise identical, the total number of elementary particles in the Standard Model does not increase [3]. Moreover, they are subject to the same interactions as the "normal" particles and they also interact between them and between each other.

2.6 Incompleteness of the SM

Despite the many successes that the Standard Model of particle physics has achieved, it is not perfect. There are still open questions and phenomena that have not been clarified. For example, the Standard Model still does not include an explanation for the fourth fundamental interaction, that is gravitation. Building on this, it has also not been possible to unite all known forces in one theory. Although it was possible to unify the electromagnetic and weak interaction by means of the $SU(2)_L$ x $U(1)_Y$ gauge groups, but the strong interaction which is described by the $SU(3)_C$ gauge group as well as gravitation have not yet been unified [15]. The combined theory of the electromagnetic, weak & strong interaction in the form of gauge groups would be the *"Grand Unified Theory"* (GUT) (Fig.2.3).

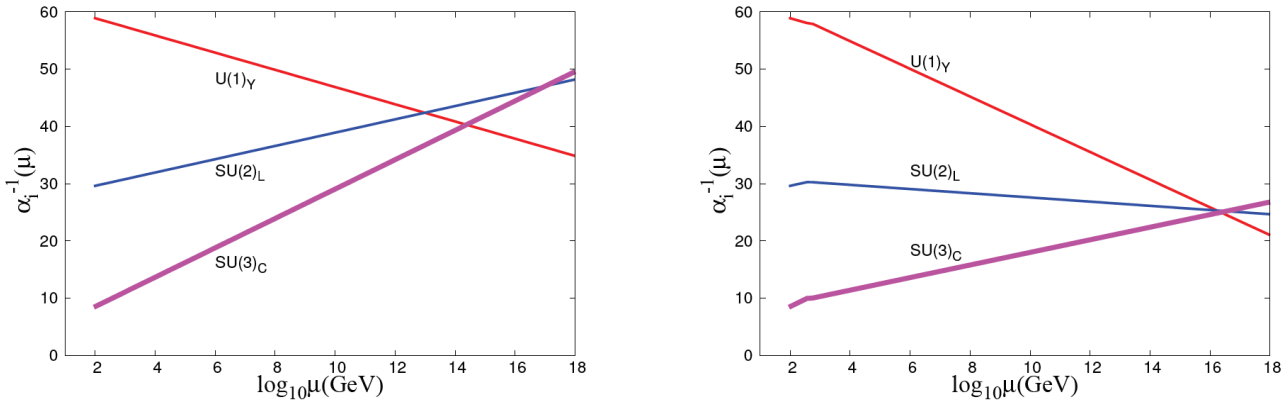

Fig. 2.3: Evolution of the three inverse fine structure constants ($\alpha_i^{-1}(\mu) = \frac{g_i^2(\mu)}{4\pi}$). **Left:** Standard Model. **Right:** Standard Model plus SUSY extension (GUT Idea of MSSM[2])[16].

So far, the smallest gauge group that unites all other groups is the $SU(5)$, whose predictions are *"close"* to the measured values but cannot fully reflect them. Further, the processes described by the Standard Model can unfortunately only explain the matter part of our universe, which accounts for about 5% of the universe based on cosmological studies. The other 95% is divided into dark matter (approx. 26%) and dark energy (approx. 69%), although theoretical models

[2]The Minimal Supersymmetric extension of the Standard Model

have been proposed to explain these, but up to now no experimental confirmation for any such model has been observed yet (Fig. 2.4).

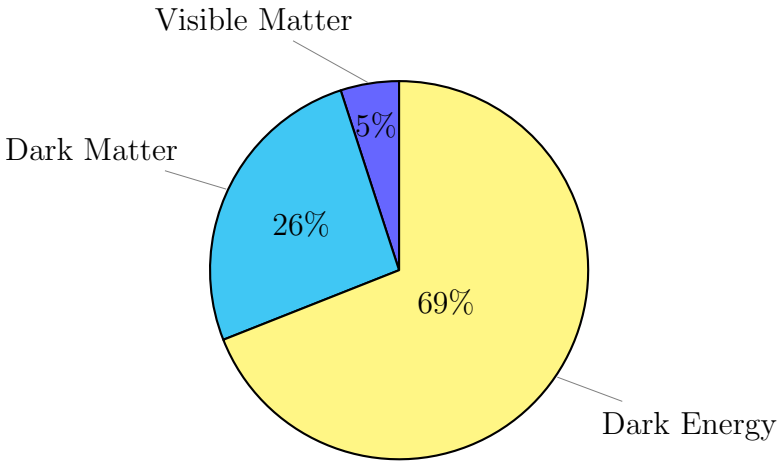

Fig. 2.4: Components of our universe [1].

There are some other aspects that are still not explained by the SM, such as the number of fermions and their mass hierarchy. The SM is not able to explain the mass of neutrinos and why there are only left-handed neutrinos. Moreover, the validity of the Standard Model still relies on nineteen free parameters. Why these parameters are as they are is still the subject of research and remains unresolved to this day.

3 Beyond the Standard Model

Following the limitations of the SM, physicists have been searching for physics phenomena that are *"Beyond the Standard Model"* (BSM). A wide variety of theories have been proposed and examined to address the inconsistencies of the Standard Model and experimental searches are being performed based on such models. Some of these theories are described below.

3.1 W′

One of the most explored BSM theories are those concerning the W' (W-prime) bosons [17–19]. These theories predict W-boson resonances of higher mass than those of the SM, with similar decay modes and branching fractions (see. SSM[1]) or right-handed versions of their original particles from a broken $SU(2)_L$ x $SU(2)_R$ symmetry [13, 21–23]. The fractional $SU(2)_L$ x $SU(2)_R$ symmetry, also $SU(2)_w$ thereby predicts by its construction $n^2 - 1$ different $W^{\pm\prime}$ and $Z^{0\prime}$ (with spin 1 & electric charge of ± 1) [13]. All these predictions of the W' boson have one thing in common, they satisfy the following Lagrangian term (Equ.3.1)[2] [21]:

$$L = \frac{g'}{2\sqrt{2}} V'_{ij} W'_{\mu} \bar{f}^{i} \gamma^{\mu} (1 \pm \gamma_5) f^{j} + H.c \tag{3.1}$$

The existence of these bosons was predicted, but they have not yet been confirmed experimentally [24, 25]. Investigations at the LHC based on data collected during proton-proton collisions at a centre-of-mass energy of $\sqrt{s} = 13$ TeV have excluded the W' boson, depending on the decay channel, for masses of up to 4.9-5.2 TeV for the SSM W′ model [23].

3.2 Sphaleron

A sphaleron is a time-independent and unstable solution of the electroweak field equations of the Standard Model of particle physics. It is involved in processes that violate baryon and lepton numbers and can not be produced at the LHC [26–28]. Within the electroweak theory ($SU(2)$) exists the idea of a vacuum structure with an infinite number of eigenstates. The periodically

[1] Sequential Standard Model [20]

[2] V'_{ij}: CKM-matrix element | W'_{μ}: four momenta of the W′ | γ^{μ}: Dirac gamma matrix | γ_5: the fifth gamma matrix | f^i: standard model fermion in the mass eigenstate basis | +H.c: plus the Hermitian conjugate

repeating eigenstates are usually represented by the so-called Chern-Simon numbers (N_{CS}) (Fig.3.1).

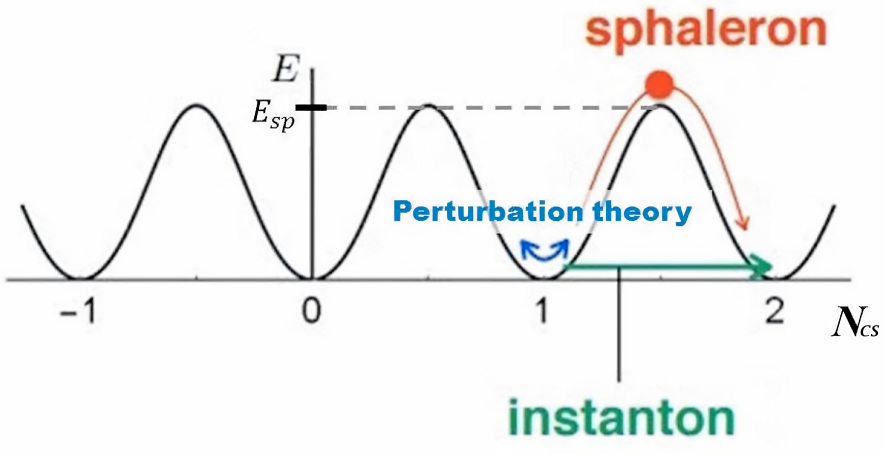

Fig. 3.1: Energy density of the gauge field as a function of Chern-Simons numbers (modified) [28].

The theory states that our universe is in one of these potential eigenstates and must pass a potential barrier of E_{sph} to get to the next eigenstate. The magnitude of E_{sph} is equivalent to the static energy solution of the hypothetical sphaleron (Equ.3.2) [28]:

$$E_{sph} = \frac{2m_W}{\alpha_W} B\left(\frac{m_H}{m_W}\right) \approx 9\ TeV \tag{3.2}$$

where m_W, m_H are W and Higgs boson masses, α_W the electroweak constant and B a tabulated function. Modern particle colliders[3] are able to reach a center of mass energy well above E_{sph} [29]. Moreover, as highlighted by S.-H. Henry Tye and Sam S. C. Wong [5, 30], sphalerons can already occur at a centre-of-mass energy below E_{sph}, but the processes are strongly suppressed. Recent searches at the CMS experiment [31] have not yet observed any signatures (like multiple jets) that would fit this model. The great interest to study the sphaleron exists partly due to their influence on the baryon number (B) and the lepton number (L). They preserve the difference (Equ.3.3), but violate their sum (Equ.3.4)[5, 28].

$$\Delta(B - L) = 0 \tag{3.3}$$

$$\Delta(B + L) = 6 \cdot \Delta N_{CS} \tag{3.4}$$

The factor "6" results from the change of the lepton and baryon number, both of which contribute with a factor "3" each [5].

[3]LHC at $\sqrt{s} = 13$ TeV

4 Experimental Setup

4.1 The Large Hadron Collider

The Large Hadron Collider (LHC) is a 27 km long particle accelerator at the European Organization for Nuclear Research (CERN) in Geneva (Fig.4.1). This makes the LHC the largest particle accelerator in the world with the largest centre of mass energy ever achieved. As the successor to the Large Electron-Positron Collider (LEP), which was closed in 2000, LHC started operating in 2008. Proton-proton collisions and lead-atom collisions are performed there. The individual particles are accelerated to speeds close to the speed of light and reach a centre of mass energy of up to $\sqrt{s} = 13$ TeV during proton-proton collisions. One of the LHC's greatest successes to date is the observation of the Higgs boson in 2012.

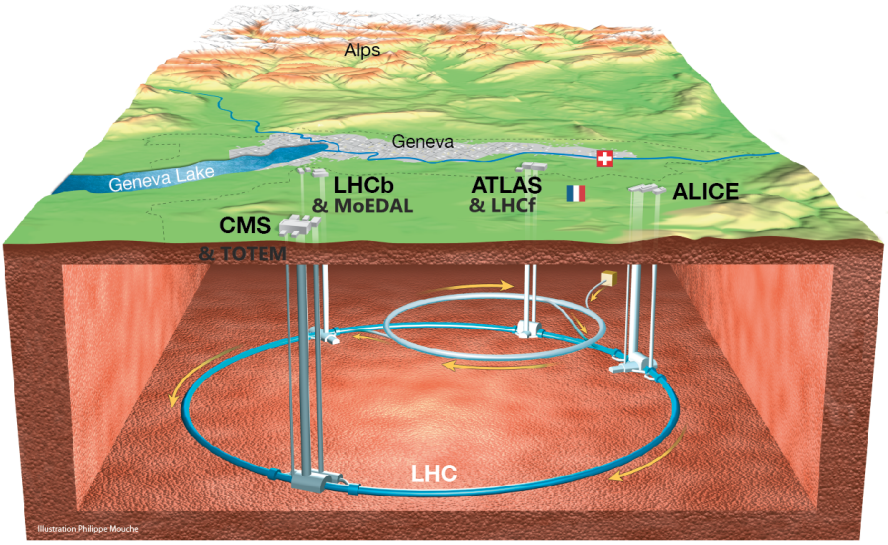

Fig. 4.1: Overall view of the LHC (modified) [32]

The particle accelerator itself is located about 50-170 m under the ground to be shielded from cosmic rays and shield the general public from hazardous side effects. A high vacuum of up to 10^{-13} bar prevails inside 5.6 cm thick tubes of the LHC to avoid unwanted collisions with air molecules. Furthermore, the system includes 1232 dipole, 392 quadrupole, 688 sextupole and 16 octupole magnets, which, with a magnetic field of up to 8.33 T, to keep the particle beams on

their circular path and focus them. To achieve such high field strengths, the superconducting magnets are cooled down to 1.5 K [7]. But the LHC does not work alone. Due to its enormous size and the fact that the LHC is a synchrotron collider, the particles must first be accelerated to a minimum entering speed. This is achieved by a chain of pre-accelerators (Fig.4.2).

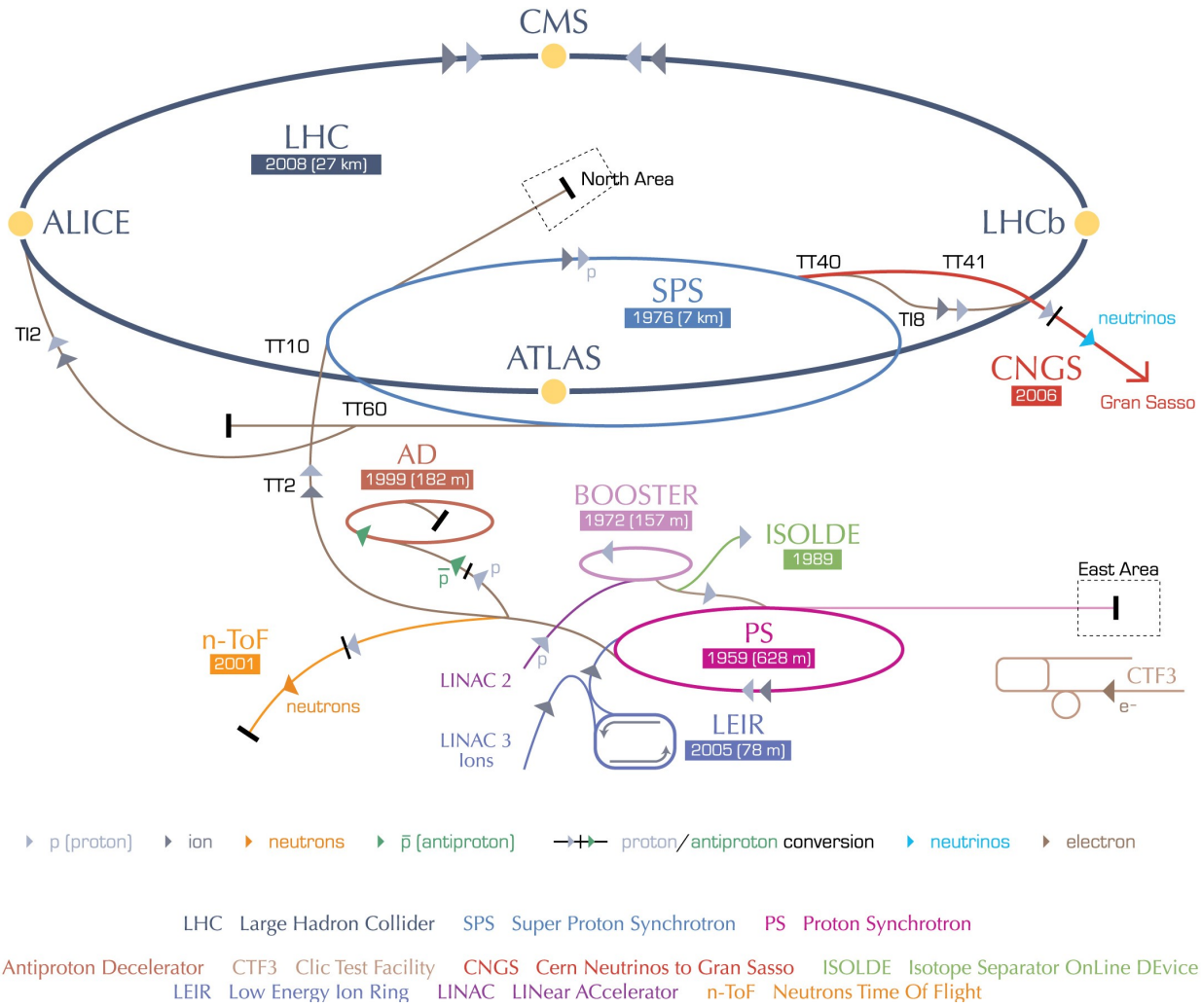

Fig. 4.2: The CERN accelerator complex (modified) [33]

In the following only the proton acceleration process will be described, because these collisions are the only ones used by the MUSiC Analysis. First, the protons are grouped into bunches and accelerated up to 50 GeV thanks to the Linear Accelerator 2 (LINAC 2). Then they pass through the Proton Synchrotron Booster (PSB), the Proton Synchrotron (PS) and the Super Proton Synchrotron (SPS). With their now collimated length of 1.35 ns, they are brought to an energy of 450 GeV. After they have reached a bunch spacing of 50 ns, they are injected into the LHC. There, each bunch reaches the final energy of 6.5 TeV [1, 5].
The main goal of LHC is to study in deep detail the fundamental particles and their interactions and to search for BSM physics phenomena. To accomplish these task, four experiments are in place at LHC [1, 4, 34]:

- **ALICE** (A Large Ion Collider Experiment): Designed to study heavy ion collisions that create conditions similar to those that occurred shortly after the Big Bang.
- **ATLAS** (A Toroidal LHC Apparatus) & **CMS** (Compact Muon Solenoid): General-purpose detectors that study proton and heavy ion collisions at extremely high energies. In doing so, they shed light on the foundations of the Standard Model and search for BSM physics, such as additional dimensions and particles that could account for dark matter.
- **LHCb** (Large Hadron Collider beauty): Specialises in the properties of b-hadrons in proton-proton collisions and aims to better understand the asymmetry between matter and antimatter in the universe.

4.2 Compact Muon Solenoid

The Compact Muon Solenoid (CMS) is one of the large LHC detectors. People working on the CMS detector and analysis are member of the CMS collaboration, which is one of the largest international scientific collaborations in history. The CMS experiment is constructed in a cylindrical form, has a diameter of about 15 m, a length of 21.6 m, weighs 14.000 tonnes and achieves a magnetic field of up to 3.8 T [4, 5, 35]. A detailed description of the CMS detector can be found in Reference [36].

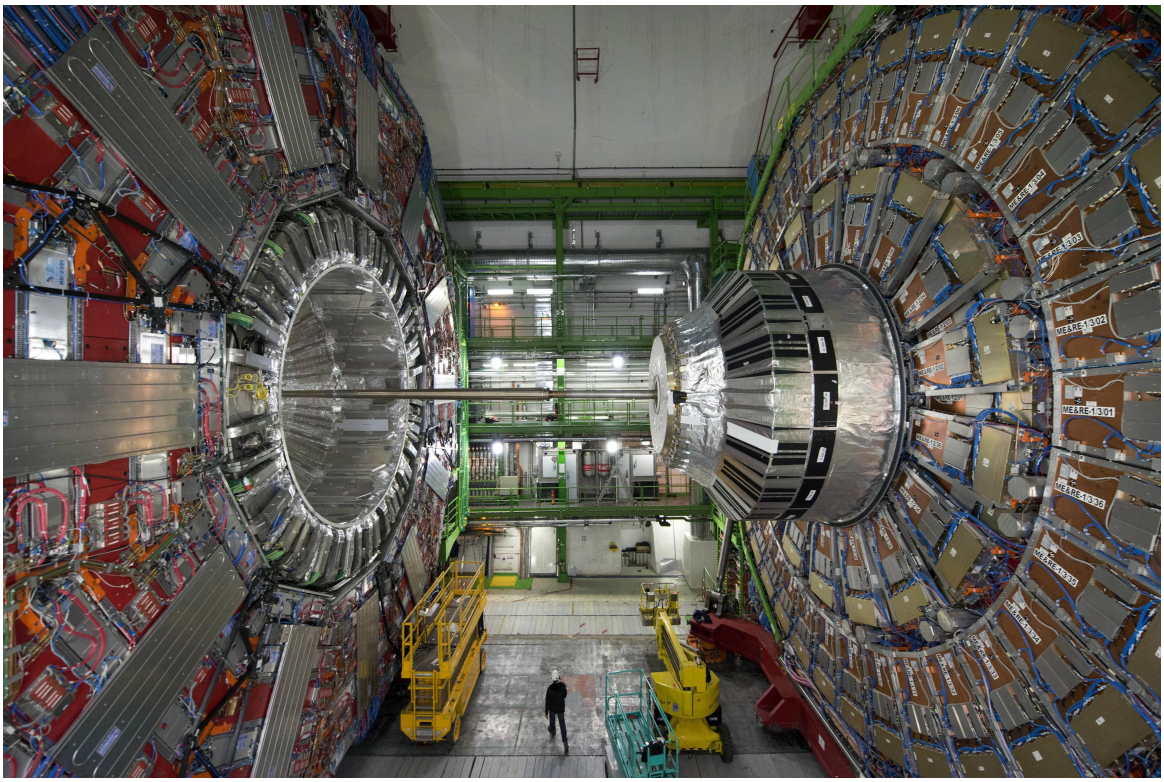

Fig. 4.3: An overview of the Compact Muon Solenoid, with a human being in the middle as a scale comparison [35]

.

4.2.1 Coordinate system of CMS

To navigate within the CMS detector, a special coordinate system is used. The origin of the coordinate system is placed in the centre of the particle collision. The x-axis points inwards, towards the LHC centre, the y-axis points upwards and the z-axis points in the direction of the beam. Like in a polar coordinate system, the radial distance r is also used here, but not the angle Θ. Instead, one uses the pseudorapidity $\eta = -\ln(\tan(\Theta/2))$ and the azimuth angle Φ, which lies in the xy-plane. This has the advantage that in the high-energy range (E$\gg$m) the eta angle becomes $\Theta = \operatorname{arctanh}(v_z/c)$ [1, 7].

4.2.2 The Detector

The detector itself is divided into two regions: the rotationally symmetric barrel section and the two endcaps. The different regions can be defined by their $|\eta|$ value (barrel region: $|\eta| < 1.4442$ & endcap region: $1.566 < |\eta| < 2.5$) [7]. Within the CMS detector, several sub-detectors were installed in order to reconstruct as many different particles as possible and to measure their physical quantities, such as momentum, mass, and energy. In addition, a two-tiered trigger system is used. It first selects events based on the information gathered by the detector at a rate of 100 kHz (in less than 4 μs) with the help of custom hardware processors and in the second step reduces the event rate for data storage to a size of 1 kHz [37]. The subdetectors present at CMS are listed below from the inner subdetector to the outer one (Fig.4.4 & Fig.4.5).

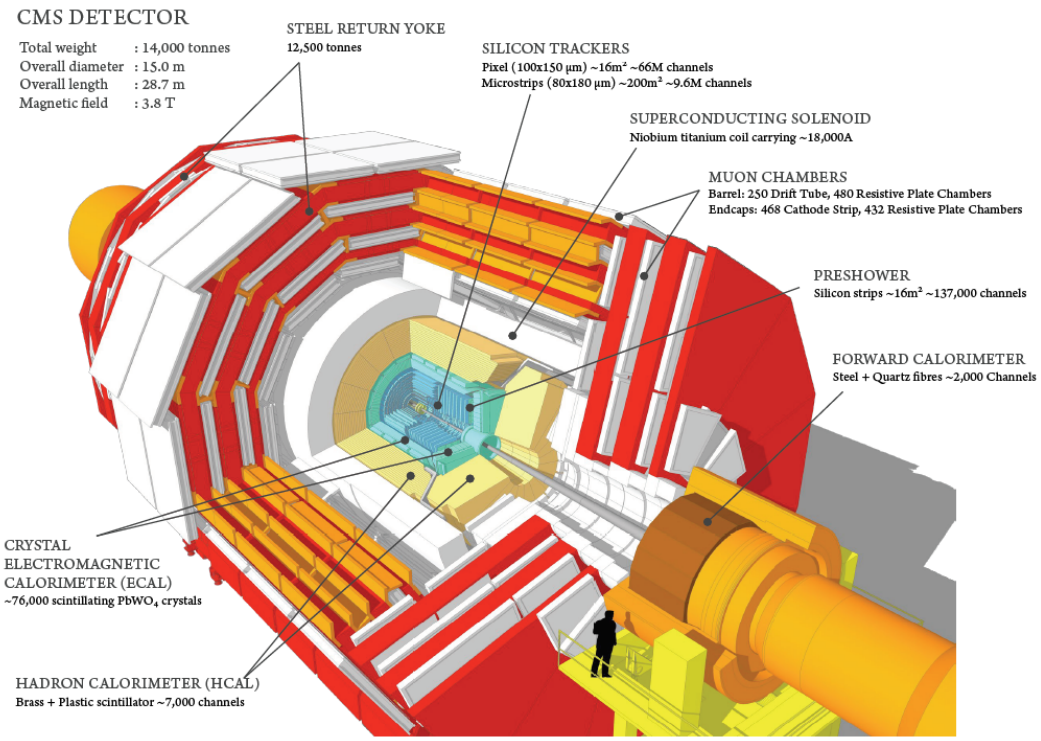

Fig. 4.4: A cutaway view of the CMS detector [38].

Pixel detector

The innermost part of the CMS detector is formed by a silicon pixel and silicon strip detector. With a pixel size of 100 μm x 150 μm (65 million pixels) and a cell size of 10 cm x 80 mm, for the silicon stripes (15.200 modules with a total of 10 million silicon stripes). They are used to measure the tracks of the particles up to $|\eta| < 2.5$ with an accuracy of 10 μm. The pixel detector occupies four barrel layers and two disks of the endcap, while the strip detector occupies ten barrel layers and twelve endcap disks.

Electromagnetic calorimeter

The electromagnetic calorimeter (ECAL) is used to measure the energy of electromagnetically interacting particles such as electrons and photons (up to $|\eta| < 3$). It consists of 80.000 $PbWO_4$ crystals. The material has been chosen because of their short radiation length. If, for example, an electron passes through the ECAL, it generates Bremsstahlung, which creates electron/positron pairs. Through the resulting shower (Fig.4.5) of particles, the electron finally releases all its energy in the ECAL. The photon energies are measured at the end of the crystal with the help of photo diodes.

Hadronic calorimeter

The hadronic calorimeter (HCAL) works in a similar way to the ECAL. In the HCAL, hadrons hit the brass part of the calorimeter and produce particle showers when they decay into other particles, which are then detected in the plastic scintillator (Fig.4.5). The measurements in the HCAL can be measured in the barrel range up to $|\eta| < 1.3$, in the endcap range up to $|\eta| < 3$ and with the components in the beam direction up to $|\eta| < 5$.

Superconducting Magnet

The next layer of the CMS is the cylindrical superconducting magnet, which generates a magnetic field of 3.8 T. This field is able to deflect the trajectory of charged particles. This deflection enables the pixel detector to measure the sign of the particle's charge as well as its momentum. Other important parts are the iron yokes, which close the magnetic flux with their three layers and act as a filter for the muon chamber (since only muons and neutrinos can still pass through the iron yokes).

Muon Chambers

The outermost and also largest layer of the CMS are the muon chambers. These were built on the very outside, since muons rarely interact within the previous layers and, together with neutrinos, they are the only particles that reach beyond the iron yokes. The muon chambers are equipped as follows:

- **Barrel region**: The barrel region ($|\eta| < 1.2$) is equipped with drift chambers and resistive plate chambers, since only a low muon rate prevails in this region.
- **Endcap region**: The highest muon rate occurs within the encap region ($0.9 < |\eta| < 2.4$), which is why cathode strip chambers are installed here in combination with resistance plate chambers.

Each of these gas based detectors work according to the same principle. Gas atoms are ionised and then release electrons that can be detected. Since several muon chambers are set up, the path of the muons can be reconstructed on the basis of the measurement positions (Fig.4.5). This method ensures that muons up to over 1 TeV can be detected with a resolution of 5% [39].

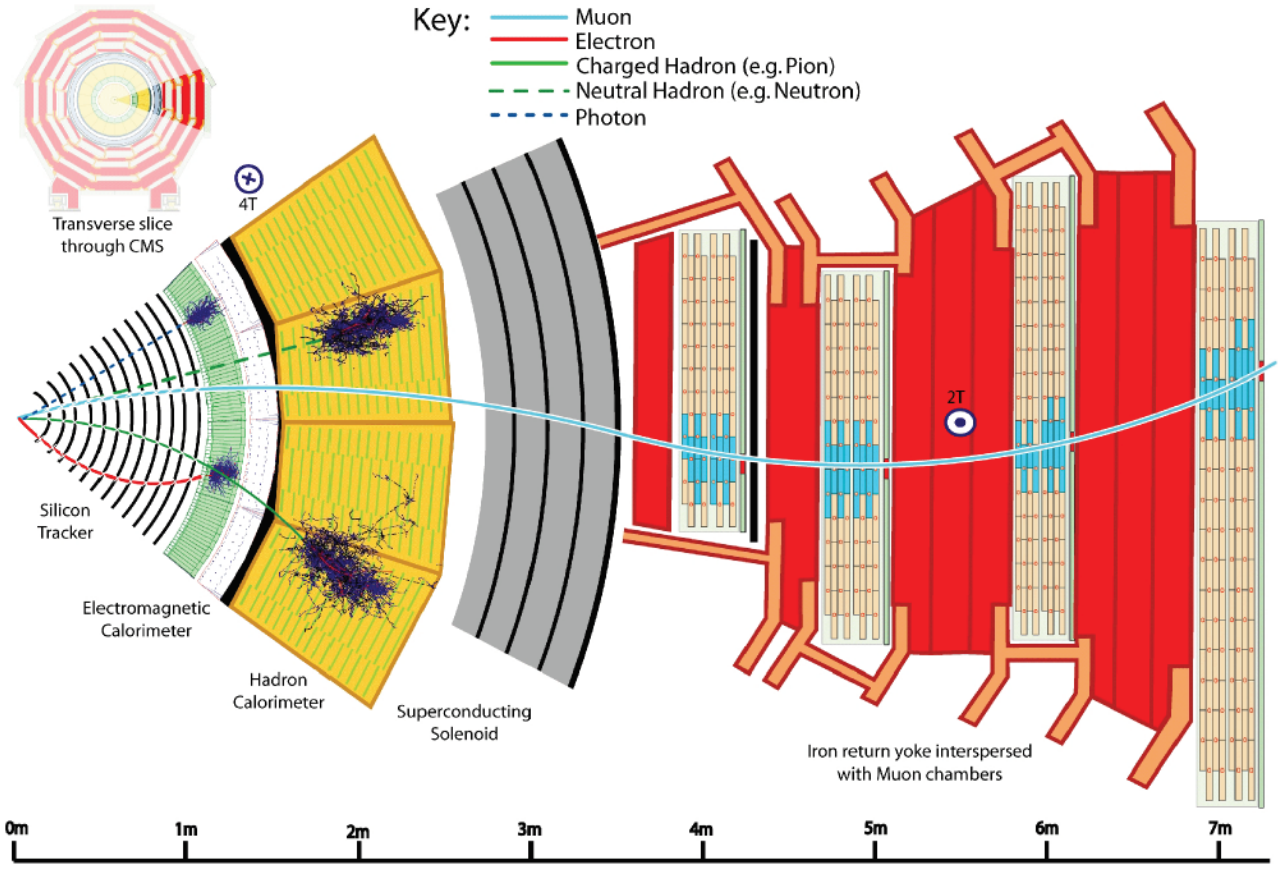

Fig. 4.5: Overview of the different subdetectors and example particles that can be measured in CMS [40].

5 MUSiC

MUSiC (Model Unspecific Search in CMS) is a general model-independent approach to search for new physics as a complementary approach to dedicated analyses for specific models in specific final states [37]. In CMS, it is not uncommon to search for new physics by looking at some (previously filtered out) final states of proton-proton collisions and analysing them according to a predicted BSM model. This kind of analysis has the advantage that it is uses a specialised approach that is specifically suited to be more sensitive to the specific BSM model(s) being probed. However, such dedicated analyses (at multiple locations) are limited by practical constraints on the computational and person power such that only a limited number of analyses can be performed leaving a large number of BSM models unexplored. In addition, there is the probability that some interesting final states are likely to remain unexplored since the analysis strategy of dedicated searches restricts them to a few specific final states that are more relevant to the particular BSM model(s) that the analysis probes. This is where the MUSiC analysis comes in. It attempts to classify the events of hundreds of different final states without model-specific filters and to examine each of these final states for deviations from the Standard Model of particle physics. With this alternative approach, one hopes to discover phenomena that are otherwise undetectable. This strategy results in a loss of sensitivity compared to the dedicated analyses. However, MUSiC can identify regions and final states where the data deviates from SM expectation and the deviation can be due to the presence of new physics phenomena, which can then be studied in detail by dedicated analyses.

5.1 Data set and simulated samples

Within the MUSiC analysis, previously recorded data from CMS at the LHC are compared with Monte Carlo (MC) simulations of the Standard Model. To obtain the Monte Carlo events, events from the generators PYTHIA 8.212, MADGRAPH5 aMC@NLO version 2.2.2, POWHEG v2 and SHERPA 2.1.1 are combined to simulate processes relevant in the SM [37]. The data sets contain the full detector information stored in physical objects and are stored on non-local parts of the computing grid. The standard data format used is the miniAOD (multiple instances) format, which provides a compact storage option to store all the information required for physics analyses. However, the data stored in this miniAOD data contains more information than MUSiC needs. Therefore, the data is first pre-processed in what is called the "skimming" step. Within this step, the miniAOD files of the measurements as well as those

of the MC simulations are shortened to the data relevant for MUSiC and saved in the .pxlio (Physics extension Library) format [1].

5.2 Object and event selection

After the "skimming" step, the object and event selection of the MUSiC workflow is performed. To reduce the impact of unwanted effects such as misidentification of particles, light conditions are placed on the data. The resulting loss of efficiency is compensated by the enormous increase in data purity. The events chosen for further analysis must contain at least one lepton (e or μ) or one photon (table 5.1), since such events can be described very well by SM simulations. The analysis requirements are slightly tighter than the trigger thresholds. If several triggers have fired, this overlap is deleted so that an event is counted only once.

Trigger used	**Trigger level requirement**	**Analysis requirement**
Single muon	1μ with $p_T > 50$ GeV	$\geq 1\mu$ with $p_T > 53$ GeV
Single electron trigger	$1e$ with $p_T > 115$ GeV	$\geq 1e$ with $p_T > 120$ GeV
Double muon trigger	1st μ with $p_T > 17$ GeV 2nd μ with $p_T > 8$ GeV	$\geq 2\mu$, each with $p_T > 20$ GeV
Double electron trigger	$2e$ with $p_T > 33$ GeV	$\geq 2e$, each with $p_T > 40$ GeV
Single photon trigger	1γ with $p_T > 175$ GeV	$\geq 1\gamma$ with $p_T > 200$ GeV

Table 5.1: Event selection criteria

The objects considered within MUSiC include e, μ, γ, jets, b-tagged jets and Missing transverse momentum (p_T^{miss} or MET), whereby in the case of particles no distinction is made based on the charge of the particles. In order to keep the efficiency of the object selection as high as possible and the misidentification rate of the individual objects as low as possible, further minimum requirements are placed on the individual objects (Table.5.2).

Object	p_T**[GeV]**	**Pseudorapidity**
Muon	> 25	$\lvert\eta\rvert < 2.4$
Electron	> 25	$0 < \lvert\eta\rvert < 1.44$ or $1.57 < \lvert\eta\rvert < 2.5$
Photon	> 25	$\lvert\eta\rvert < 1.44$
Jet	> 50	$\lvert\eta\rvert < 2.4$
b-tagged jet	> 50	$\lvert\eta\rvert < 2.4$
MET	> 100	-

Table 5.2: Object selection criteria

These selection requirements are for the objects used in the analysis in general, but for the objects that are associated with the trigger, the requirements are mentioned in the table 5.1. Should these criteria again identify an object as two or more particles, the following procedure is applied. First, the particles are sorted in the order e, μ, γ and jets. This is done exactly in this order, as it is assumed that it also corresponds to the sequence of purity. Then, if there

is ambiguity within this list, the object that has the highest priority is selected and the other particles that are close in distance to $\Delta R = \sqrt{(\Delta\eta)^2 + (\Delta\Phi)^2} = 0.4$ (or $\Delta R = 0.5$ for jets) are removed from the event.

5.3 Classification

After the data has been selected, events are stored into different event classes. MC events are weighted to normalize the luminosity of the observed data set based on the cross section of the physic process. Once this is done, the observed data as well as the MC events are divided into different event classes depending on their physical objects. The different types of event classes considered are (Fig.5.1):

1. **Exclusive classes**: The exclusive class contains only the events that have exactly the physics objects as specified in the label of the event class (e.g. $1e$+2μ+1jet). The result is that each event is always assigned to only one exclusive class.

2. **Inclusive classes**: The inclusive classes contain events that include a nominal set of selected objects and may contain additional objects. Thus, an event is usually assigned to several inclusive classes. As an example, the event $1e$+2μ+1jet is assigned to the inclusive classes 2μ+X, $1e$+X, $1e$+1μ+X, etc. The +X stands for any number of additional objects.

3. **Jet-inclusive classes**: The third event class is the jet-inclusive event class. This was added to make the MUSiC analysis more robust against occurring radiation, which can originate e.g. from emerging gluons, but does not change the intrinsic physical process. The class contains the objects of the final state under investigation as well as an arbitrary number of jets (e.g. $1e$+2μ+1jet+Njets). However, since simulation of events with five or more jets does not describe the data accurately, all events with five or more jets are classified in the X+5 jets jet-inclusive event classes.

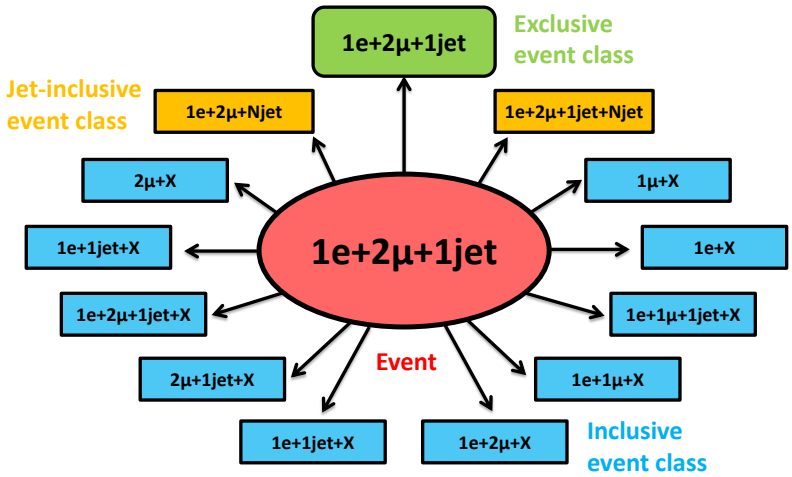

Fig. 5.1: Example of a single MUSiC event classification of an $1e$+2μ+1jet event.

Then, event classes without data and with an MC event yield of less than 0.1 are not considered for further analysis. For the processes explained later, the exclusive classes are statistically independent and uncorrelated with each other due to their composition. All other correlations between the inclusive classes were taken into account and the statistical fluctuations of the MC simulated events were assumed to be negligible.

5.4 The Scan

After all the events have passed the classification process, the analysis reaches the "scan" step. The goal of the scan step is to compare observed data with the simulation of the SM in each event class and to identify major deviations.

5.4.1 Kinematic distributions

The scan is performed on three kinematic distributions to the CMS event and MC events. These three were chosen for their sensitivity to be BSM phenomena. Moreover, the fact that only three kinematic distributions are considered, ensures that the analysis is not overly complex and time-consuming. The distributions considered are as follows:

1. **Sum of transverse momenta (S_T)**: The sum of transverse momenta of all the particles in an event is determined as the first kinematic distribution. This is the most general one among the three distributions to be considered and is determined for each event class analysed. As the name suggests, S_T is the scalar sum of all N object transverse momenta and is determined as follows (equ.5.1):

$$S_T = \sum |\vec{p}_T| \equiv \sum_i^N |\vec{p}_{T,i}| \tag{5.1}$$

   Since heavy particles are often postulated within BSM theories, a close look at S_T is extremely interesting, since if they exist they should be seen within the tails of the S_T distribution.

2. **Combined mass (M)**: The second distribution is the combined mass M. Usually, the combined mass is the invariant mass (M_{inv}).

$$M_{inv} = \sqrt{\tilde{E}^2 - \tilde{p_x}^2 - \tilde{p_y}^2 - \tilde{p_z}^2} \tag{5.2}$$

   Where $\tilde{E}$ is the sum of the particle energy and $\tilde{p_x}$, $\tilde{p_y}$, $\tilde{p_z}$ are the sums of the momentum components. However, since p_T^{miss} is still present in many classes, the transverse mass

(M_T) is used instead of the invariant mass. This is because in these cases the momentum component in the beam direction cannot be measured precisely enough to determine M_{inv}.

$$M_T = \sqrt{\tilde{E_T}^2 - \tilde{p_x}^2 - \tilde{p_y}^2} \tag{5.3}$$

With $\tilde{E_T}$ as the sum of the transverse particle energy. With a precondition that the considered event classes contain at least two objects, the combined mass is helpful to draw conclusions about massive particles.

3. **Missing transverse momentum (p_T^{miss})**: The third kinematic distribution considered is the missing transverse momentum, defined here as the negative vector sum of the four-vector transverse momenta (equ.5.4).

$$p_T^{miss} \equiv | - \sum_i^N \vec{p}_{T,i}| \tag{5.4}$$

p_T^{miss} is used to determine the energy that could not be detected by the detectors. Within this distribution, only classes with at least $p_T^{miss} \geq 100$ GeV are considered. This limit was chosen because low values of p_T^{miss} are due to neutrinos predicted in the SM or detector resolution effects.

When determining the distributions for each event class, only the particles that are explicitly mentioned in the event class are taken into account. This means, for example, that for the class 1e+2μ+X only the electron and the two muons are taken into account. In the case that a particle occurs several times within a class, e.g. in a $1e$+X class there is a second electron event, the particle with the largest p_T value is considered in the distribution. Another important point to consider is the bin width of the kinematic distributions. If this is not optimally adjusted, unwanted effects can occur. A large bin width has the advantage of reducing the computing time required for evaluation, but the analysis loses sensitivity. A small bin width, on the other hand, is susceptible to letting random fluctuations influence the analysis too much. The goal is therefore to find a middle ground between these two extremes. As a solution, an automatic adaptation of the bin width to the typical overall resolution of the detector for all objects in each specific kinematic range was chosen. As a result, a larger value for the bin width is chosen for higher energies than for smaller ones. Therefore, the bin widths are finally chosen to be integer multiples of 10 GeV.

5.4.2 p-Value

The next step of the analysis is the determination of p-values. The p-value is the probability of how well the simulations and the observed data agree. A hybrid Bayesian-frequentist approach

is used. In order to be able to describe the statistical fluctuations as well as possible, a Poisson distribution was chosen as the probability of making N_{data} observations (equ.5.5):

$$P(N_{data}) = \frac{e^{-N_{SM}} N_{SM}^{N_{data}}}{N_{data}!} \tag{5.5}$$

With N_{SM} as the number of events expected from the SM simulations. So that the possible extreme cases (surpluses or deficits of observed data compared to the expected value) can also be considered within the investigation. This Poisson distribution is further summed up (equ.5.6).

$$p = \begin{cases} \sum_{i=N_{data}}^{\infty} \frac{e^{-N_{SM}} N_{SM}^{i}}{i!} & \text{, if } N_{data} \geq N_{SM} \\ \sum_{i=0}^{N_{data}} \frac{e^{-N_{SM}} N_{SM}^{i}}{i!} & \text{, if } N_{data} < N_{SM} \end{cases} \tag{5.6}$$

Obviously the mean of the Poisson distribution is not exactly known. Therefore, a Gaussian distribution with a width of $\sigma_{SM} = \sqrt{\sigma_{MC,stat}^2 + \sigma_{MC,sys}^2}$ around N_{data} is used (equ.5.7).

$$p_{data} = \begin{cases} \sum_{i=N_{data}}^{\infty} C \int_0^{\infty} d\lambda \exp\left(-\frac{(\lambda - N_{SM})^2}{2\sigma_{SM}^2}\right) \frac{e^{-\lambda}\lambda^i}{i!} & \text{, if } N_{data} \geq N_{SM} \\ \sum_{i=0}^{N_{data}} C \int_0^{\infty} d\lambda \exp\left(-\frac{(\lambda - N_{SM})^2}{2\sigma_{SM}^2}\right) \frac{e^{-\lambda}\lambda^i}{i!} & \text{, if } N_{data} < N_{SM} \end{cases} \tag{5.7}$$

Here C is the normalisation factor of the Gaussian distribution. All the distributions in the previous steps are then divided into regions. The regions are defined as any contiguous combination of bins and reach a number of $N_{bins}(N_{bins}+1)/2$[1]. A p-value is now determined for each of these regions (Fig.5.2). The smallest p-value obtained for the different regions is considered for that distribution (p_{data}).

[1] N_{bins} = Number of bins

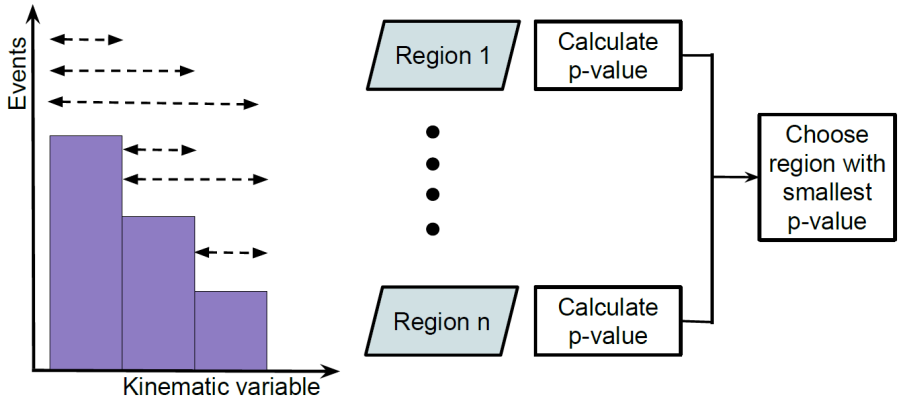

Fig. 5.2: Schematic representation of the determination of the p-values of each region and the related selection of the region with the smallest p-value.

Once this is done, the lowest p-value is sought, which defines the region of interest (RoI). This is, after the definition of the p-value, the region that shows the largest deviations between measured and simulated data (Fig.5.3).

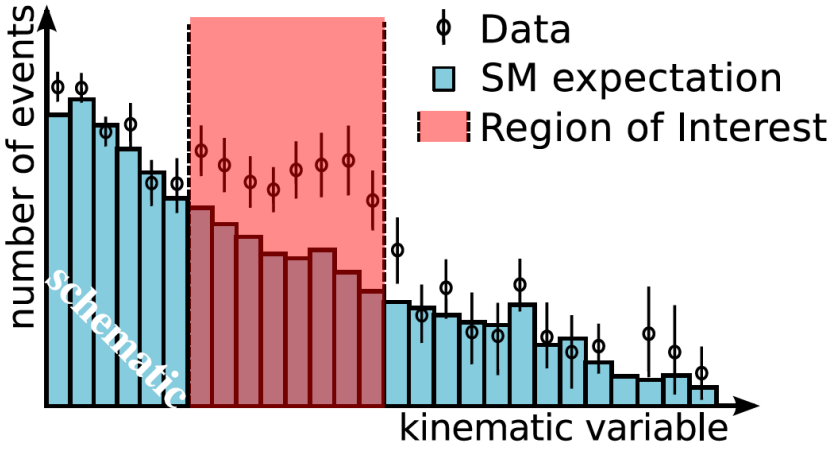

Fig. 5.3: Illustration of the RoI within one of the kinematic distributions (modified) [4].

In order to reduce possible statistical fluctuations, a minimum number of bins within a region is set when determining the regions. These are set as three for S_T and p_T^{miss} and as one for M. In addition, all regions that have too few simulated events are removed. This gives a probability distribution for each kinetic variable (S_T, M, p_T^{miss}).

5.4.3 Look elsewhere effect and the $\tilde{p}$-value

Before the RoI can be determined as described in the previous section, an additional effect must be considered. Since the determination of the p-value refers to the comparison of individual regions, it is only able to reflect a local deviation of the data. However, a global comparison of data and simulation is desired. This difference is also called the "Look-Elsewhere Effect"

(LEE) [41]. In order to correct for the effects of the LEE and thus be able to describe a global distribution of all regions, a new value is determined, the $\tilde{p}$-value. Since the deviations of the regions are strongly correlated, the $\tilde{p}$-value used is estimated as accurately as possible. In the process, a series of pseudo-experiments are created that also go through all the previous steps. In order to achieve the highest possible sensitivity and at the same time avoid enormous computing time, up to 10.000 pseudo-experiments are created during this process. The smallest p-value (p_{min}^{data}) resulting from the comparison of the measured data with the MC simulations serves as a reference. All locally smallest p-values (p_{min}) of the pseudo-experiments are then counted, added up and divided by the total number of comparisons. The value obtained in this way is the $\tilde{p}$ value (equ.5.8).

$$\tilde{p} = \frac{N_{pseudo}(p_{min} < p_{min}^{data})}{N_{pseudo}} \tag{5.8}$$

In this type of determination, which is a statistical estimate of how likely it is to see a deviation at least as strong as the observed one in some region of the distribution, it may happen that no p_{min} are found that are smaller than p_{min}^{data}. In such a case, an upper bound for the $\tilde{p}$ value is used, since no matter how improbable an event is, its probability can never be exactly zero. Therefore, in the case of N pseudo experiments, a bound of $\tilde{p}$-value is $\tilde{p} = \frac{1}{N}$.

5.5 Dicing

When creating the pseudo experiments of an event class distribution, values for each bin must be generated so that they are very similar to the ensemble of expected values under the pure simulation hypothesis (null hypothesis). To achieve this, the mean expected values $\langle N_n \rangle$ in each bin are shifted slightly using two methods. This procedure is called "dicing". First, the systematic uncertainties (Table 5.3) of the null hypothesis are represented by a set of perturbation parameters ν_i.
It is assumed that all nuisance parameters are fully correlated across all bins. In order to do so, it is assumed that the systematic uncertainties have been separated to a level where the underlying processes responsible for the uncertainty remain similar within the entire range under consideration in a distribution. The effect of each nuisance parameter is modelled with a Gaussian distribution, centred on the mean expectation value for each bin n. To account for the correlation effect mentioned earlier, a random number κ_i is created (diced) for each perturbation parameter ν_i, which follows a standard normal distribution. At this point the first shift occurs according to the following formula (equ.5.9):

$$\langle N_{n,shifted} \rangle = \langle N_n \rangle + \sum_{i=1}^{N_{\nu_i}} \kappa_i \cdot \delta_{\nu_{i,n}} \tag{5.9}$$

where $\langle N_{n,shifted} \rangle$ is the shifted mean of each bin, N_{ν_i} is the number of all perturbation param-

Source of uncertainty	Typical values
Integrated luminosity	2.5%
Pileup	<5%
Cross sections of SM processes	For processes calculated at LO: 50% For higher-order calculations: varies, <50%
Parton distribution functions	Following PDF4LHC [42] recommendations
Value of α_S	Variations of ± 0.0015 around central value (0.118)
Electron, muon, and photon energy scales	0.15–7.00%
Jet energy scale and resolution	3-5%
Unclustered energy	Varies, typically 0–15 GeV
Reconstruction and identification efficiency	Varies, <10%
Misidentification uncertainties	50%
MC statistical uncertainty	Varies, up to 30%

Table 5.3: Summary of systematic uncertainties in the analysis [37].

eters considered and $\delta_{\nu_{i,n}}$ is the difference between the mean and the upper/lower bound of the confidence interval. Following this, the second method starts immediately, where $\langle N_{n,shifted} \rangle$ is shifted again. This is done because usually the number of events in a bin may still be slightly shifted due to statistical effects. To include this effect, one uses a Poisson distribution with $\langle N_{n,shifted} \rangle$ as the mean to smear it. The result of this is the final value used in the pseudo experiment. However, this procedure only comes into effect when the bins have an MC expectation and an expected contribution from nuisance parameters. For bins with no MC expectation or no contribution from uncertainties, this shift procedure is omitted.

5.6 Global overview

In order to combine all the results of the event classes and kinematic distributions, it was decided to present them in the form of histograms. The distributions of the deviations in the event classes are compared with the expected distribution of the SM only hypotheses obtained from pseudo experiments. The advantage of such a display is that both scenarios, where a BSM signal shows a large deviation in a few individual final states and also the case when a BSM signal shows small deviations but in several final states, can be observed. The $\tilde{p}$ distributions are first determined for all pseudo-experiments, as described in the previous analysis step (5.4.2 & 5.4.3).

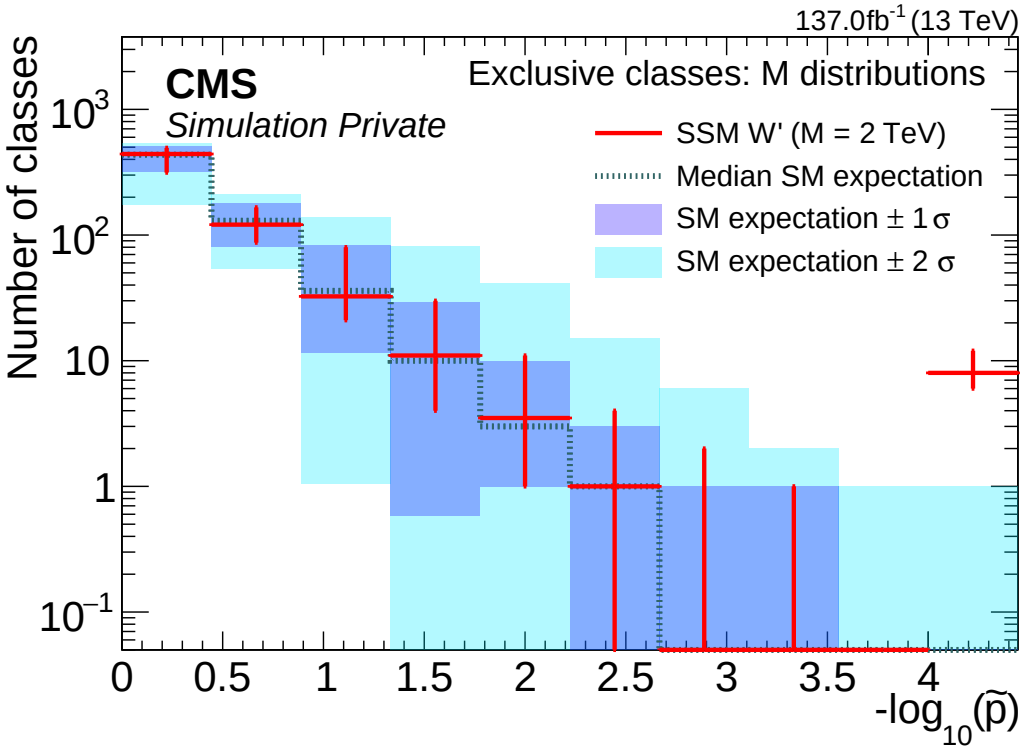

Fig. 5.4: Illustrative example of a $\tilde{p}$-value distribution (of a W′ analysis) for different classes (final states) based on a RoI scan for the MUSiC analysis.

The histogram in Fig.5.4 shows an example based on a result of this analysis. The number of classes is plotted against their matching $\tilde{p}$-values, which is shown here in $-\log_{10}(\tilde{p})$ steps for the sake of clarity. The construction of the histogram for the SM expectation begins by taking the median of the pseudo experiment distributions for each bin as a reference for the SM hypothesis. In order to additionally obtain the uncertainty in the SM only hypothesis distribution, one and two sigma deviations with respect to the median, two coloured areas are displayed around the median corresponding to the bands containing the distributions of 68% (resp. 95%) of the pseudo-experiments. Due to this type of generation, the size of the areas above and below the median may differ, as within the pseudo-experiments the concentration of event numbers in different dicing rounds may be different. The distribution obtained for the scan of the signal under consideration is shown as the histogram displayed as the red crosses on top of the histograms for the SM only hypothesis. A red cross outside of the SM expectation like the one on the right site of Fig.5.4 illustrates a deviation from the SM that cannot be explained by fluctuations and is an indication of a BSM signal. It should also be noted that the systematic errors estimated in Section 5.5 may still influence the $\tilde{p}$ distributions used for the histogram, resulting in more event classes showing smaller deviations and appearing in the bins with the smallest deviations. To incorporate this, the uncertainty bands used were increased by studies of pseudo-data to include an overestimation of uncertainty up to 50%. However, this has no effect on the range where very large deviations are expected and where evidence for BSM effects is hoped for.

6 Signal Studies

6.1 Introduction

In order to demonstrate MUSiC's capabilities, sensivity studies on the current state of the algorithm are carried out regularly. It will be the focus of this bachelor thesis. During the sensivity studies, no data previously recorded by CMS is examined, but pseudo-data corresponding to particular BSM models, which were usually created to fit certain BSM theories. Such a signal is superimposed on a previously generated SM-MC simulation and used as a data set. This approach does not change the model unspecific approach of MUSiC, since the analysis is not filtered or adapted to a specific model, but only sensitivity tests lead to these. Such investigations have the advantage that it becomes clear, which parameters a signal must have in order to be recognised by MUSiC. Additionally it is possible to calculate the limits within MUSiC is able to detect a BSM signal. Since one compares simulations of BSM signals with SM-MC simulations here, one can, in contrast to the usual procedure, carry out an investigation of an event several times, since all data can be regenerated at any frequency. This has the consequence that within the sensitivity study, approximate values for the uncertainties of the $\tilde{p}$-distribution are obtained by carrying out the analysis several times. These become noticeable in the form of error bars in the "Median signal rounds" representation (red markings) (Fig.5.4) within the histograms.

6.2 Results of the analysed signals

For the following sensitivity studies, the luminosity was increased from 35.9 fb^{-1} to 137.0 fb^{-1} corresponding to the data set collected by CMS during LHC Run 2 which is expected to be analysed by the MUSiC algorithm in the next iteration of the analysis. In addition, the BSM theories of W′ and sphaleron described in the chapter 3 were investigated.

6.2.1 Results of the W′ signal

For the W′ investigation, a localised excess of events in particular final states is expected, Therefore, it is highly probable to see a resonance in the M_{inv} distribution (Fig.6.2). As described in the sequential standard model (SSM)[20], this would be an indication of a heavy W boson that promptly decays into a charged lepton and a neutrino (Fig.6.1).

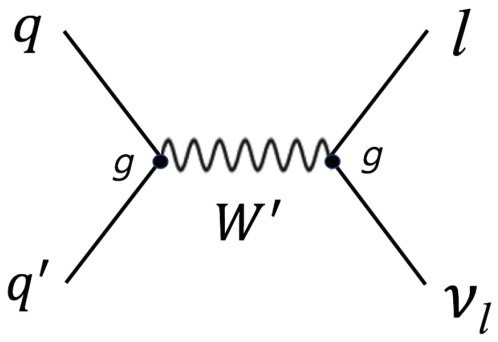

Fig. 6.1: Production and decay of a new heavy W′ boson (modified)[23]

A typical signature for a possible W′ generation would be an event containing a single isolated, energetic charged lepton, a substantial p_T^{miss} and an arbitrary number of jets originating from the radiation in the initial or final state. The analysis generates up to 10.000 pseudoexperiments under an SM-only hypothesis and takes into account of the LEE in each distribution and event class. The results of the scan for the M_{inv} (or M_T) distribution of the exclusive event class serve as a representative of the investigation of the W′. Hypothetical masses of 2, 3, 4 & 5 TeV for the W′ boson were investigated. A distribution of the W′ signal with 3 TeV mass and SM background is shown in Figure 6.2.

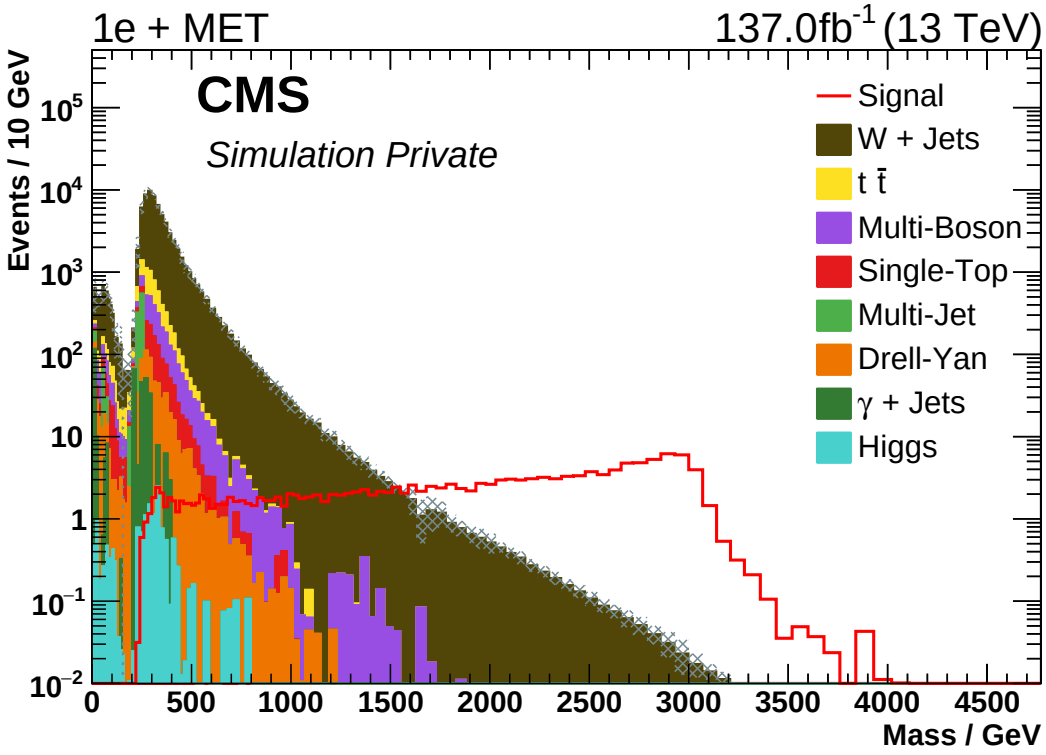

Fig. 6.2: Distribution of the transverse mass of a hypothetical W′ ($M_{W'} = 3$ TeV) for the $1e$+MET exclusive class.

In addition to this distribution (as described in section 5.6), global overviews of the $\tilde{p}$ distributions were generated in the form of histograms (Fig.6.3) (further plots can be found in the appendix (chapter 11.1)).

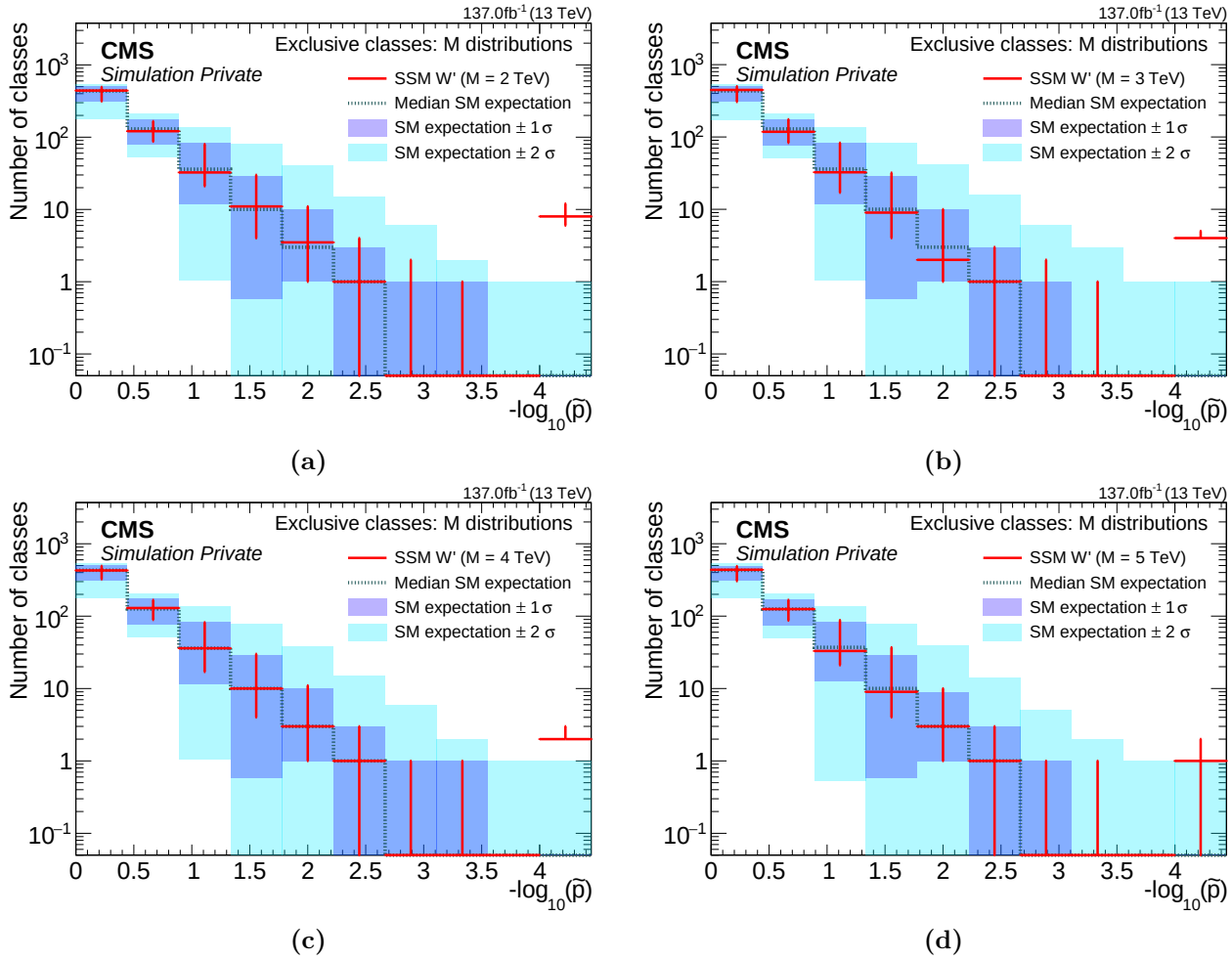

Fig. 6.3: Histograms of the $\tilde{p}$-values for the kinematic distribution M_{inv} for different W′ masses. The overviews of the W′ 2 TeV (a), 3 TeV (b), 4 TeV (c) and 5 TeV (d) measurements are shown.

It can be noticed that different event classes present a very low $\tilde{p}$-value. This is illustrated by the red marker (median signal rounds SSM W′) in the last bin of each histogram. It is very clear that the number of classes with such low $\tilde{p}$-values is well above the SM expectations. Therefore, these excesses are produced by the injected BSM signal. Moreover, the number of classes contained within this possible BSM signal decreases more and more as the W' mass ($M_{W'}$) increases. At the largest $M_{W'}$ value considered (Fig.6.3d) it ends at 1-2 classes for the lowest $\tilde{p}$-value. Thus the associated bin is just outside the 95% of SM range. These event classes are listed in table 6.1 showing the event classes with $\tilde{p}$-values less than 0.01, which correspond to larger deviations. Based on the pseudo data sets, there are more or less event classes, which gives the uncertainty of the red makers. This in turn results in some of the markers having no error bars in one of the directions.

	Event Class	p	$\tilde{p}$	RoI [GeV]	N_{pseudo}	$N_{SM} \pm \sigma_{SM}$
$M_{W'} = 2$ TeV	$1e$+MET	10^{-8}	$< 10^{-5}$	980 - 1070	624	210 ± 41
	$1e$+1γ+MET	10^{-8}	$< 10^{-5}$	1540 - 1660	19	1,4 ± 0,78
	1μ+MET	10^{-8}	$< 10^{-5}$	810 - 950	1446	770 ± 89
	1μ+1γ+MET	10^{-8}	$< 10^{-5}$	1220 - 1370	35	4,8 ± 2,5
	$1e$+1Jet+MET	10^{-8}	$< 10^{-5}$	1720 - 1880	807	300 ± 64
	1μ+1Jet+MET	10^{-8}	$< 10^{-5}$	1630 - 1860	1583	740 ± 130
	$1e$+2γ+1Jet+MET	$1{,}1 \cdot 10^{-5}$	0,0001	1660 - 2520	3	0,03 ± 0,02
	$2e$+MET	$9{,}5 \cdot 10^{-6}$	0,0003	1620 - 1760	8	0,49 ± 0,43
	$1e$+1bJet+MET	0,00039	0,01	1820 - 2300	42	10 ± 7,3
$M_{W'} = 3$ TeV	$1e$+MET	10^{-8}	$< 10^{-5}$	1830 - 1980	41	10 ± 2,4
	$1e$+1Jet+MET	10^{-8}	$< 10^{-5}$	2720 - 2950	70	15 ± 4,8
	1μ+MET	10^{-8}	$< 10^{-5}$	1350 - 1660	178	87 ± 8,9
	1μ+1Jet+MET	10^{-8}	$< 10^{-5}$	2380 - 2810	332	86 ± 38
$M_{W'} = 4$ TeV	$1e$+MET	10^{-8}	$< 10^{-5}$	3140 - 3360	8	0,21 ± 0,043
	1μ+MET	10^{-8}	$< 10^{-5}$	2120 - 2890	37	10 ± 1,3
	$1e$+1Jet+MET	$7 \cdot 10^{-6}$	0,0015	3890 - 4190	9	0,64 ± 0,51
$M_{W'} = 5$ TeV	$1e$+MET	10^{-8}	$< 10^{-5}$	4020 - 4380	4	0,015 ± 0,0082
	1μ+MET	$1{,}6 \cdot 10^{-6}$	0,0023	3280 - 5410	6	0,31 ± 0,067

Table 6.1: Overview of the most significant event classes in the RoI scan for the kinematic distribution M_{inv} for $M_{W'}$ = 2 - 5 TeV in the sensitivity study. p is the median p-value of several pseudo-experiments, $\tilde{p}$ is the p-value corrected with the LEE, RoI represents the limits of the region of interest (described in section 5.4.2), N_{pseudo} is the number of pseudo-data events and $N_{SM} \pm \sigma_{SM}$ is the number of events expected from the SM simulations.

For a W′ mass of 2 TeV there are several event classes (9) showing significant deviation beyond the SM expectation with $\tilde{p} < 0.01$, 7 of the event classes with $\tilde{p} < 0.0001$ and each of them are of the type of one lepton+MET+number of jets (or photons), which are consistent with the expected signal from the W′ boson. This demonstrates the capability of MUSiC to identify deviating classes correctly, based on the expectation of the W′ signal. Further looking at higher W′ masses, the number of event classes with large deviations becomes smaller (4 for $M_{W'}$ = 3 TeV, 3 for $M_{W'} = 4$ TeV and 2 for $M_{W'} = 5$ TeV), following the expectation of a reduced cross section of the signal at higher W′ masses. It can be seen, even up to masses of 5 TeV that MUSiC is able to identify event classes showing large deviations for the scenario of a luminosity of 137.0 fb^{-1} of the analysed data set.

Improvements in the W′ measurement

The results carried out by this analysis with an integrated luminosity of 137.0 fb^{-1} have been compared to the results carried out on the 2016 data set with an integrated luminosity of 35.9 fb^{-1} [37]. Figure 6.4 shows a comparison between the global overview histogram carried out by this analysis and the older one. The histograms of the W′, with a mass of 2-4 TeV show a slightly increased number in their most significant event classes (from 3-4 in the analysis corresponding to 35.9 fb^{-1} of data to 4-5 in the analysis corresponding to 137.0 fb^{-1} of data).

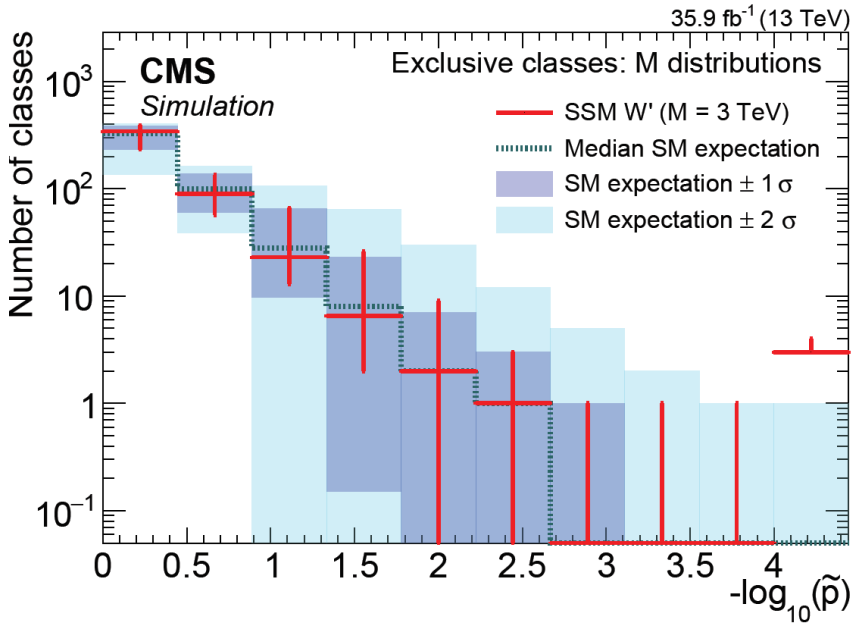

(a)

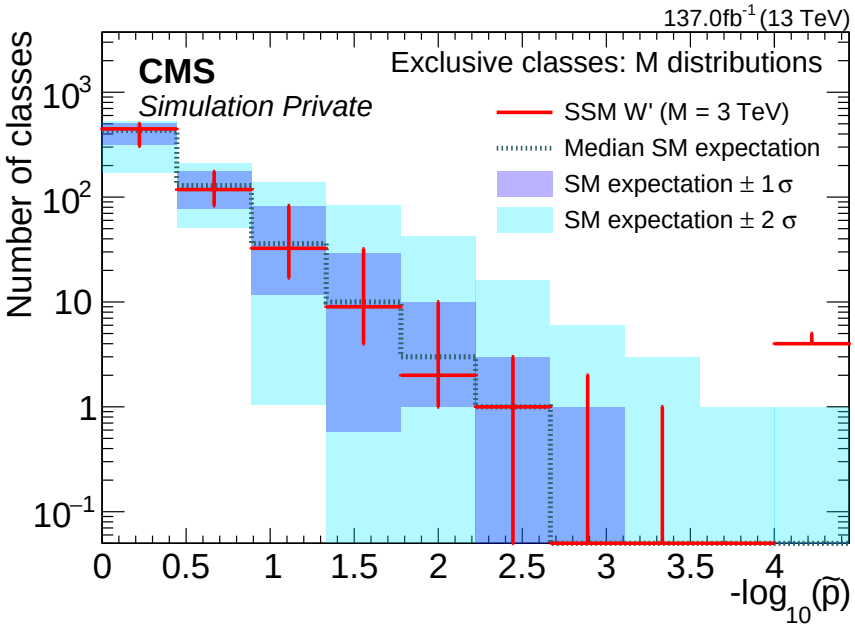

(b)

Fig. 6.4: Histograms of $\tilde{p}$-values for the kinematic distribution M_{inv} for $M_{W'} = 3$ TeV analysis corresponding to 35.9 fb^{-1} of data [37] (a) and analysis corresponding to 137.0 fb^{-1} of data (b).

Moreover, thanks to the increased luminosity, it is now possible to detect a signal at a mass of 5 TeV (Fig.6.5). This is an improvement of the sensitivity in the W′ detection of 1 TeV, which is significant as this region was previously undetectable.

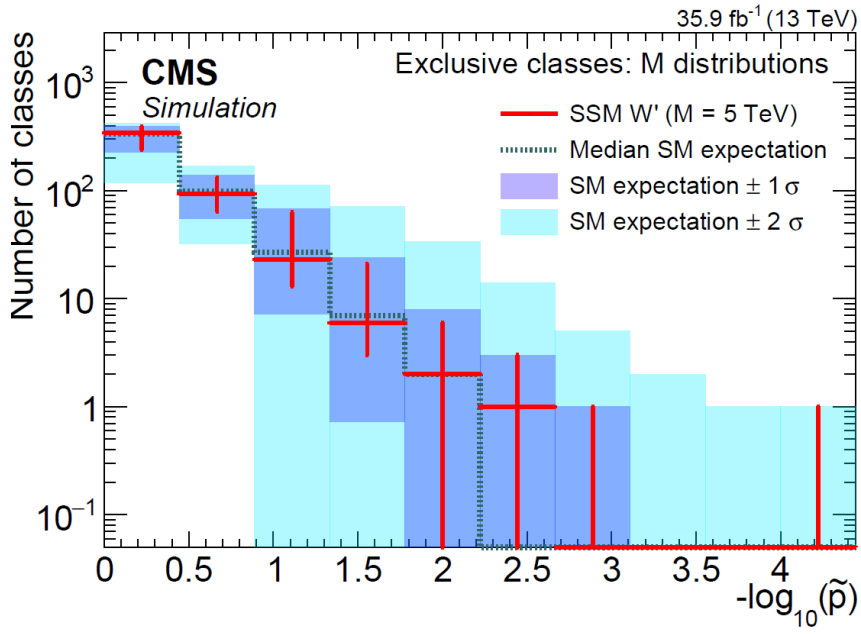

(a)

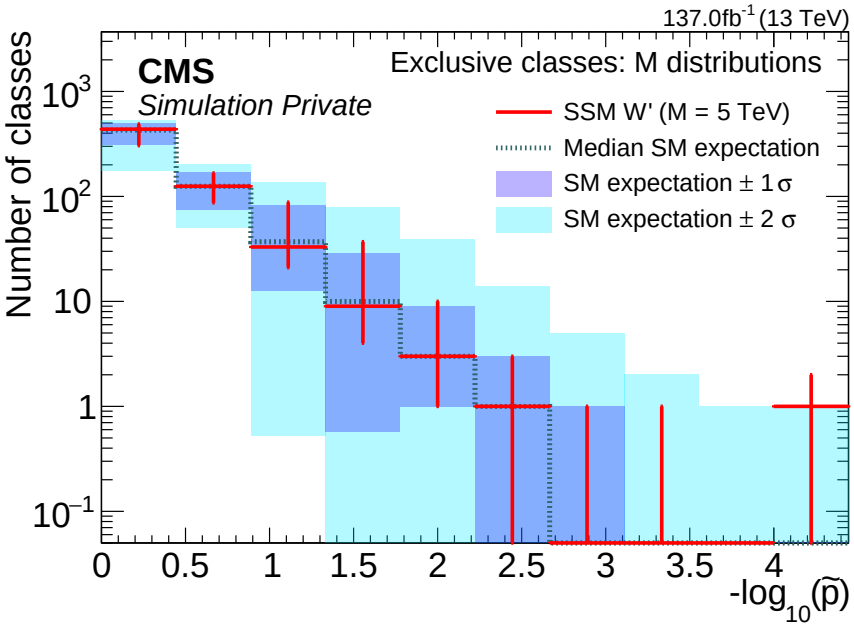

(b)

Fig. 6.5: Histograms of $\tilde{p}$-values for the kinematic distribution M_{inv} for $M_{W'} = 5$ TeV analysis corresponding to 35.9 fb^{-1} of data [37] (a) and analysis corresponding to 137.0 fb^{-1} of data (b).

6.2.2 Results of the sphaleron signal

In contrast to the W′ investigation, the analysis of the sphaleron signal is expected to have an effect in the tail of the S_T distribution. This is the reason why the following analyses concentrate on this distribution. The sphaleron signal investigated here was generated at a treshold of $E_{sph} = 8$ TeV at LO with the BARYOGEN v1.0 generator [43] with the CT10 LO PDF set [44]. Signals to various preexponential factors (PEF) were investigated within MUSiC. The PEF is of particular interest because it is related to the cross section (σ) of the sphaleron, defined as the fraction of all quark-quark interactions above the sphaleron energy threshold E_{sph} that undergo the sphaleron transition (equ.6.1) [37, 45].

$$\sigma = PEF \cdot \sigma_0 \tag{6.1}$$

with $\sigma_0 = 121\ fb$ for $E_{sph} = 8$ TeV. For the sphaleron signal, PEFs of 0.01, 0.02, 0.025 & 0.05 were investigated within the RoI scan. A distribution of the Sphaleron signal with PEF = 0.01 is shown in Figure 6.6.

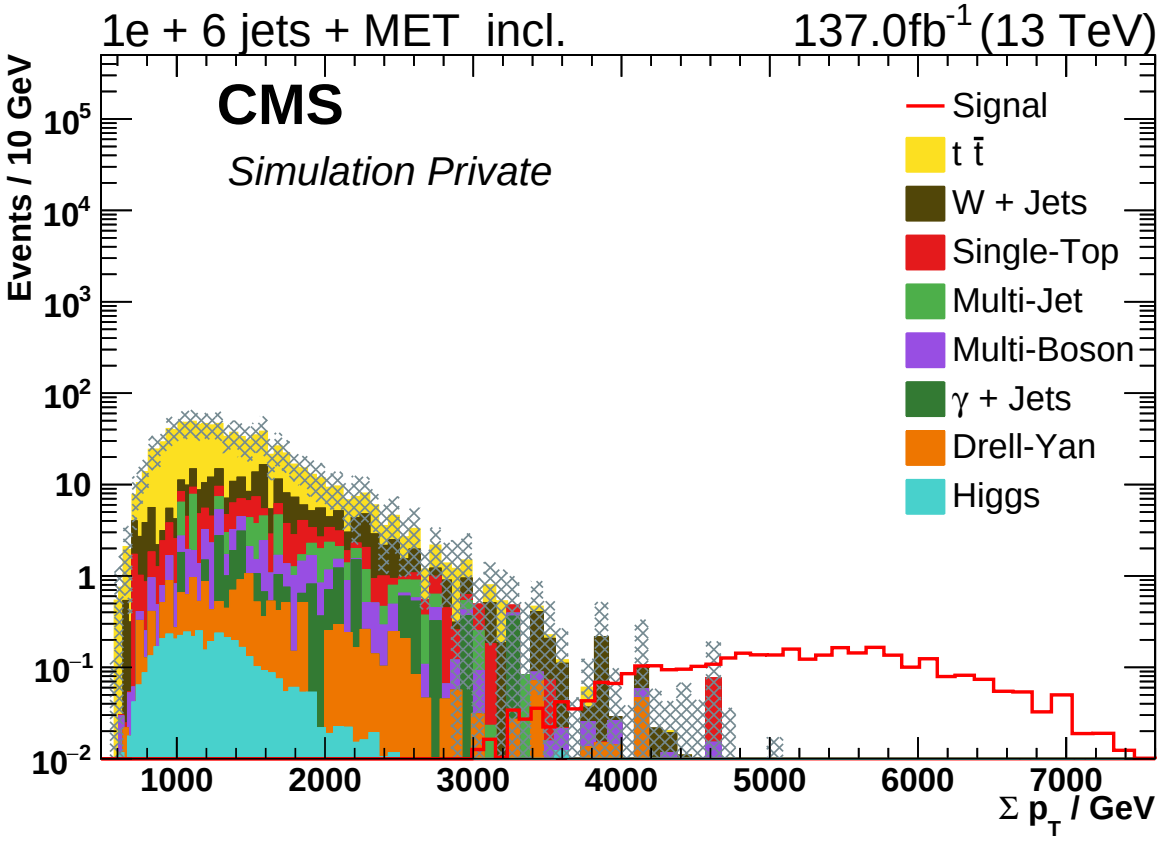

Fig. 6.6: Distributions of S_T of a hypothetical Sphaleron with PEF = 0.01 for the $1e$+6Jet+MET+X inclusive class.

In Fig.6.7 a global overview of the results of the inclusive event classes of the Sphaleron signal is shown (further plots can be found in the appendix (chapter 11.2)).

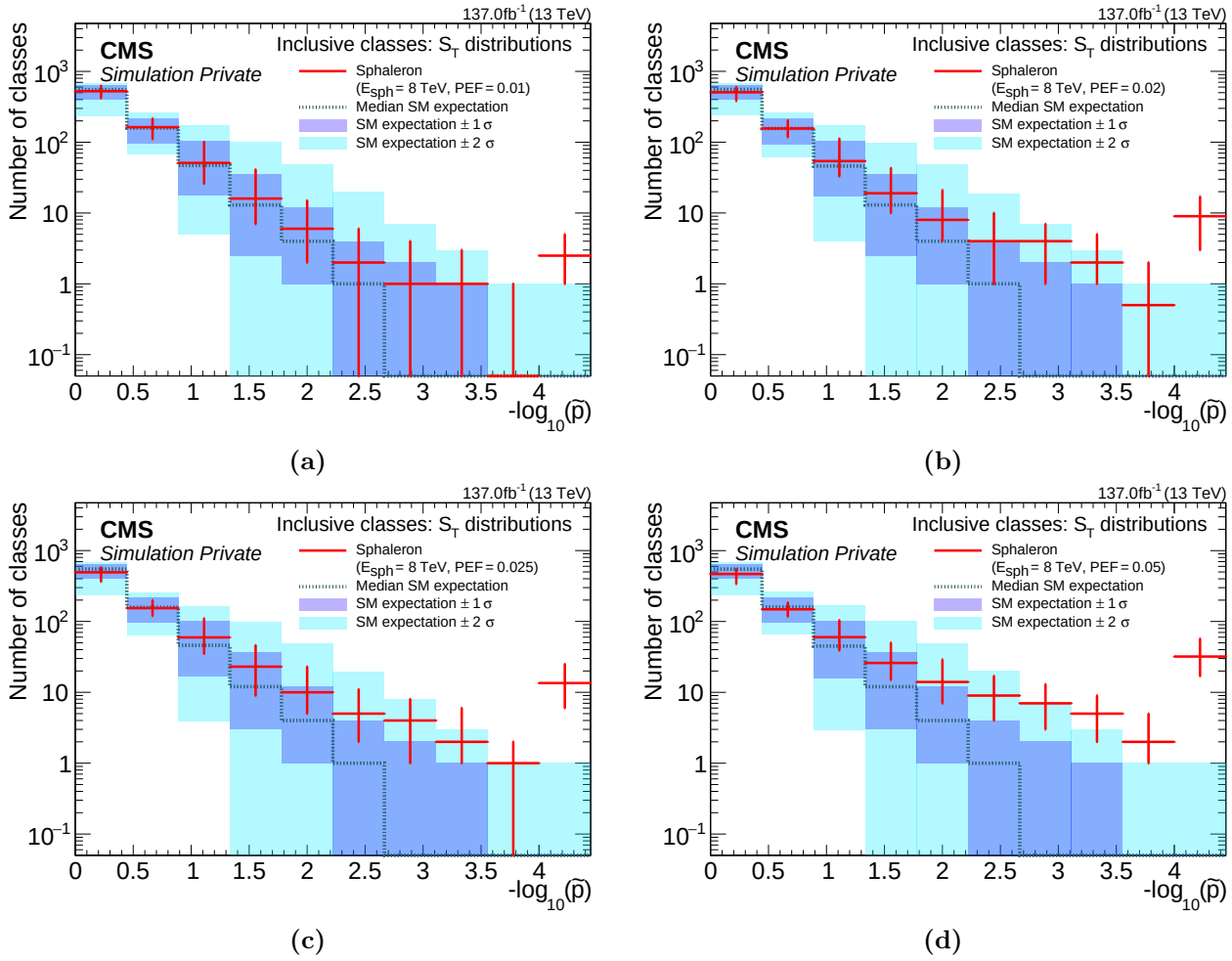

Fig. 6.7: Histograms of the $\tilde{p}$ values for the kinematic distribution S_T for different PEF. The overviews of the PEF = 0.01 (a), 0.02 (b), 0.025 (c) and 0.05 (d) measurement are shown.

It can be seen that for all PEFs considered (0.01-0.05) MUSiC is able, as in the W′ investigation, to obtain a larger value for the "median of signal rounds" (red marker) than expected from the SM. Thus MUSiC is able to detect the sphaleron signal within this PEF. A close examination of the most deviating event classes (table 6.2) revealed one event class in particular. The event classes $1e$+6Jet+MET+X, 2μ+6Jet+X and $1e$+1μ+5Jet+X (table 6.2) belongs to the event classes with the greatest deviation from the SM prediction in the smallest PEF considered. The $\tilde{p}$ distributions were shown in figure 6.7 where the entries in the right most bin present the event classes showing large deviations beyond the expectation. These event classes are listed in table 6.2 showing the event classes with $\tilde{p}$-value less than 0.01, which correspond to larger deviations.

	Event Class	p	$\tilde{p}$	RoI [GeV]	N_{pseudo}	$N_{SM} \pm \sigma_{SM}$
PEF = 0.01	$1e$+6Jet+MET+X	10^{-8}	$< 10^{-5}$	6010 - 6900	6	$1{,}5{\cdot}10^{-5} \pm 1{,}3 \cdot 10^{-5}$
	2μ+6Jet+X	$5{,}5{\cdot}10^{-6}$	0,0004	5620 - 6910	1	$4{,}3{\cdot}10^{-6} \pm 4{,}2 \cdot 10^{-6}$
	$1e$+1μ+5Jet+X	$5{,}1{\cdot}10^{-5}$	0,0015	2600 - 6680	19	2,7 ± 2,4
PEF = 0.02	$1e$+6Jet+MET+X	10^{-8}	$< 10^{-5}$	6010 - 6900	13	$1{,}5{\cdot}10^{-5} \pm 1{,}3 \cdot 10^{-5}$
	$1e$+1μ+5Jet+X	10^{-8}	$< 10^{-5}$	2600 - 4920	29	2,7 ± 2,4
	$1e$+2bJet+1Jet+MET+X	$1{,}9{\cdot}10^{-6}$	$< 10^{-5}$	4740 - 5070	1	$1{,}6{\cdot}10^{-6} \pm 1{,}4 \cdot 10^{-6}$
	1μ+1bJet+2Jet+MET+X	$6{,}2{\cdot}10^{-7}$	0,0002	4050 - 6320	42	7 ± 4,8
	1μ+1bJet+3Jet+X	$1{,}5{\cdot}10^{-6}$	0,0002	3720 - 5980	55	11 ± 6,9
	$1e$+1μ+1bJet+1Jet+MET+X	$1{,}2{\cdot}10^{-5}$	0,0002	2550 - 5200	22	2,9 ± 2,5
	$1e$+1μ+3Jet+MET+X	$1{,}5{\cdot}10^{-5}$	0,0003	2880 - 6590	41	8,6 ± 5,4
	$1e$+1μ+1bJet+3Jet+X	$5{,}5{\cdot}10^{-6}$	0,0004	2410 - 5040	25	4 ± 2,7
	$1e$+1bJet+2Jet+MET+X	$9{,}5{\cdot}10^{-6}$	0,0005	3830 - 5310	27	3,7 ± 3,4
	2μ+6Jet+X	$4{,}3{\cdot}10^{-6}$	0,0007	5620 - 6130	1	$3{,}6{\cdot}10^{-6} \pm 3{,}1 \cdot 10^{-6}$
PEF = 0.025	$1e$+6Jet+MET+X	10^{-8}	$< 10^{-5}$	6010 - 6900	12	$1{,}5{\cdot}10^{-5} \pm 1{,}3 \cdot 10^{-5}$
	2μ+6Jet+X	10^{-8}	$< 10^{-5}$	5620 - 6130	2	$3{,}6{\cdot}10^{-6} \pm 3{,}1 \cdot 10^{-6}$
	$1e$+1μ+5Jet+X	10^{-8}	$< 10^{-5}$	2600 - 5050	30	2,7 ± 2,4
	1μ+1bJet+3Jet+X	$2{,}3{\cdot}10^{-8}$	$< 10^{-5}$	3720 - 6890	64	11 ± 6,9
	1μ+1bJet+2Jet+MET+X	$3{\cdot}10^{-8}$	$< 10^{-5}$	3910 - 6320	60	10 ± 6,4
	$1e$+1bJet+2Jet+MET+X	$1{,}3{\cdot}10^{-7}$	$< 10^{-5}$	3830 - 5310	33	3,7 ± 3,4
	$1e$+1μ+1bJet+3Jet+X	$2{,}2{\cdot}10^{-7}$	$< 10^{-5}$	2410 - 6600	29	4 ± 2,7
	$1e$+1μ+3Jet+MET+X	$7{,}3{\cdot}10^{-7}$	$< 10^{-5}$	2880 - 7360	47	8,6 ± 5,4
	$1e$+2bJet+1Jet+MET+X	$1{,}9{\cdot}10^{-6}$	$< 10^{-5}$	4740 - 5070	1	$1{,}6{\cdot}10^{-6} \pm 1{,}4 \cdot 10^{-6}$
	$1e$+1μ+1bJet+1Jet+MET+X	$1{,}9{\cdot}10^{-6}$	$< 10^{-5}$	2630 - 5420	23	2,9 ± 2,3
PEF = 0.05	$1e$+2bJet+1Jet+MET+X	10^{-8}	$< 10^{-5}$	4740 - 5070	6	$1{,}6{\cdot}10^{-6} \pm 1{,}4 \cdot 10^{-6}$
	$1e$+6Jet+MET+X	10^{-8}	$< 10^{-5}$	6010 - 6900	25	$1{,}5{\cdot}10^{-5} \pm 1{,}3 \cdot 10^{-5}$
	2μ+6Jet+X	10^{-8}	$< 10^{-5}$	5620 - 6130	2	$3{,}6{\cdot}10^{-6} \pm 3{,}1 \cdot 10^{-6}$
	1μ+1bJet+2Jet+MET+X	10^{-8}	$< 10^{-5}$	4530 - 5100	54	1,9 ± 1,7
	$1e$+1μ+1bJet+1Jet+MET+X	10^{-8}	$< 10^{-5}$	2630 - 3280	29	2,9 ± 2,2
	$1e$+1μ+2Jet+X	10^{-8}	$< 10^{-5}$	2450 - 3220	47	5,8 ± 4,5
	$1e$+1bJet+2Jet+MET+X	10^{-8}	$< 10^{-5}$	3830 - 4630	42	3,6 ± 3,3
	$1e$+1μ+2bJet+1Jet+MET+X	10^{-8}	$< 10^{-5}$	2360 - 3520	14	0,68 ± 0,59
	1μ+3Jet+MET+X	10^{-8}	$< 10^{-5}$	4050 - 5310	132	23 ± 14
	$1e$+1μ+5Jet+X	10^{-8}	$< 10^{-5}$	2600 - 3900	31	2,7 ± 2,4

Table 6.2: Overview of the most significant event classes in the RoI scan in inclusive classes for the kinematic distribution S_T for a sphaleron signal with PEF = 0.01, 0.02, 0.025 & 0.05 in the sensitivity study. p is the median p-value of several pseudo-experiments, $\tilde{p}$ is the p-value corrected with the LEE, RoI represents the limits of the region of interest (described in section 5.4.2), N_{pseudo} is the number of pseudo-data events and $N_{SM} \pm \sigma_{SM}$ is the number of events expected from the SM simulations.

For the sphaleron model the signal gives rises of multiple physics objects and such the sensitivity is more pronounced in the inclusive event classes, hence the scan performed for the inclusive event classes. The deviations often are seen in regions with small MC expected yield. For PEF of 0.05 there are several event classes (10) showing significant deviation beyond the SM expectation with $\tilde{p} < 10^{-5}$ and each of them are of the type of one or two leptons+MET+number of jets+X, which are consistent with the expected signal from a sphaleron. This demonstrates again the capability of MUSiC to identify deviating classes correctly, based on the expectation of a sphaleron signal. Further looking at the lowest sphaleron PEF (0.01), the number of event classes with large deviations becomes smaller (3), following the expectation of a reduced cross section of the signal at lower sphaleron PEFs. It can be seen, even up to PEFs of 0.01 that MUSiC is able to identify event classes showing large deviations for the scenario of a luminosity of 137.0 fb^{-1} of the analysed data set.

Improvements in the Sphaleron measurement

MUSiC has thus also had success in researching the Sphaleron signals during the past year by increasing the luminosity within the analysis.
As before with the W′ results, the histogram of the Sphaleron, with a PEF of 0.05 show a increased number in its most significant event classes (from 4-30 in the analysis corresponding to 35.9 fb^{-1} of data to ca. 20-60 in the analysis corresponding to 137.0 fb^{-1} of data).

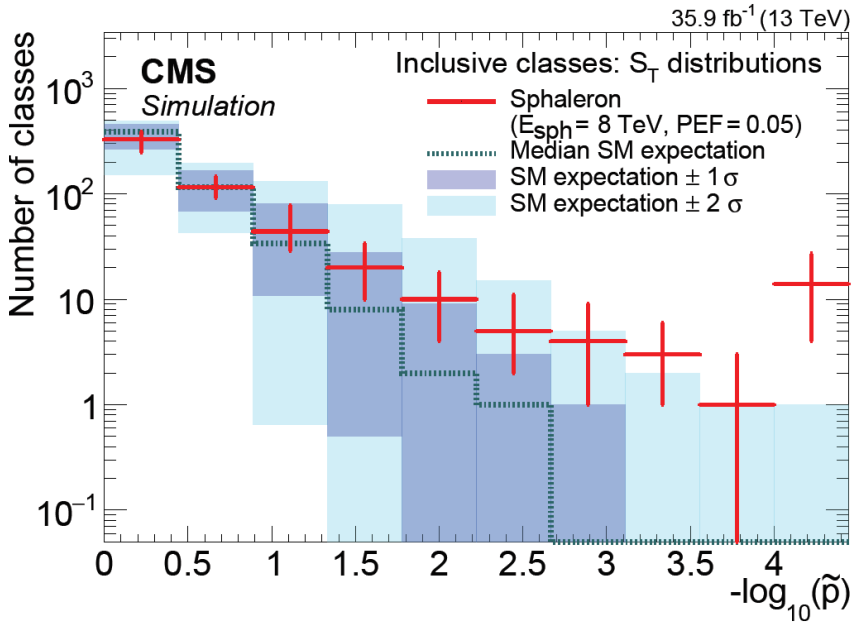

(a)

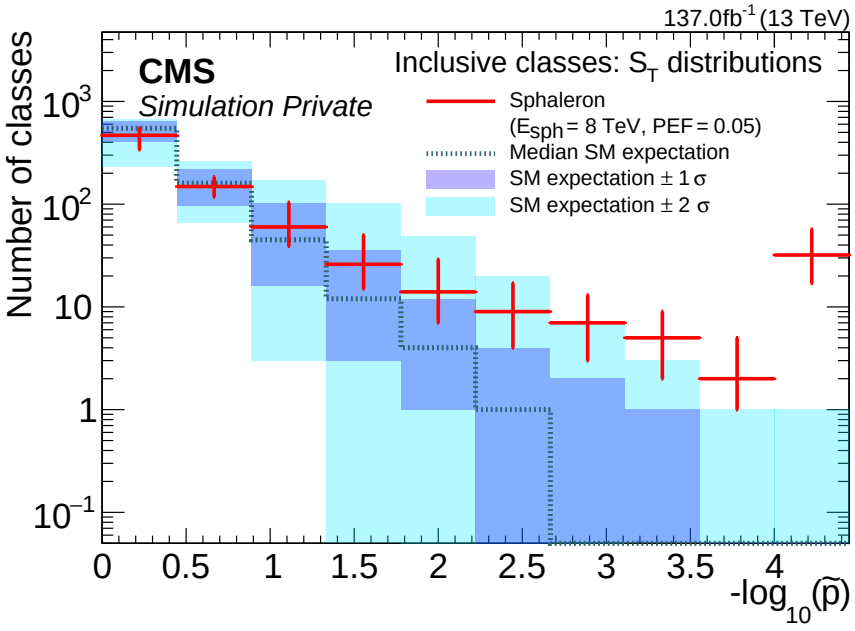

(b)

Fig. 6.8: Histograms of $\tilde{p}$ values for the kinematic distribution S_T for PEF = 0.05 analysis corresponding to 35.9 fb^{-1} of data [37] (a) and analysis corresponding to 137.0 fb^{-1} of data (b).

In contrast to last year, when the lowest PEF considered was PEF = 0.05, even smaller values have now been examined and signals with a PEF = 0.01 are now also recognisable (Fig.6.9).

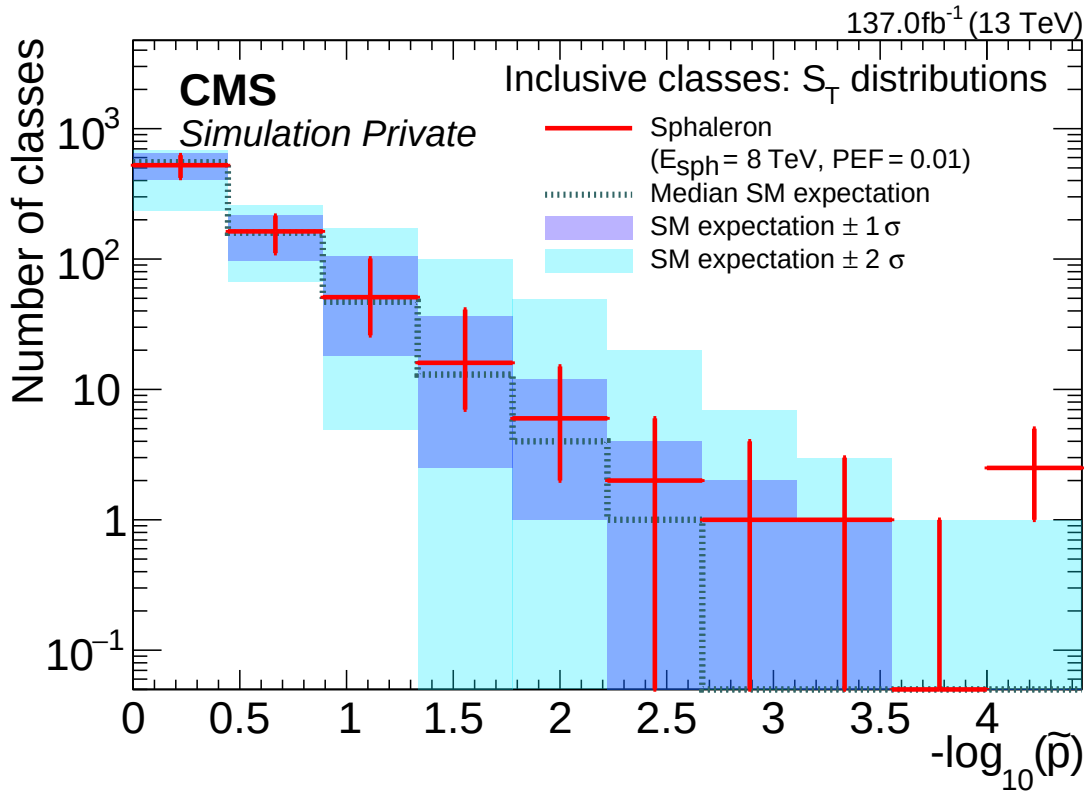

Fig. 6.9: Histogram of $\tilde{p}$-values for the kinematic distribution S_T for PEF = 0.01 of the Sphaleron study corresponding to 137.0 fb^{-1} of data.

Since within the global overview histogram of the Sphaleron signal with a PEF = 0.01 the number of classes for the lowest $\tilde{p}$-value is 1-5, the limit for the lowest possible PEF value observable with MUSiC will be slightly below 0.01.

7 Conclusion

The studies carried out in this thesis has again demonstrated the capability of MUSiC through several sensitivity studies using simulations of the Standard Model background and certain BSM models corresponding to the data collected by the CMS experiment during proton-proton collisions at a center-of-mass energy of 13 TeV at the CERN LHC. MUSiC is sensitive to W′ and sphaleron MC signals and is able to detect them up to a mass of $M_{W'} = 5$ TeV and PEF = 0.01 within the $\tilde{p}$-plots. Moreover, compared to the previously reported results, a larger mass limit for the W′ (from $M_{W'} = 4$ TeV to $M_{W'} = 5$ TeV) and a lower PEF limit (from PEF = 0.05 to PEF = 0.01) for the sphaleron study became accessible due to the luminosity increase from 35.9 fb^{-1} to 137.0 fb^{-1}. Therefore, the sensitivity study of this thesis provides a good basis to achieve even better results than before in future MUSiC analyses.

8 Outlook

Now that the Sensitivity Study within this bachelor thesis has been successful from our own point of view and has delivered promising results, there are two big events coming up next. The first is the next step of the MUSiC team, which will carry out a complete analysis and evaluation of the data set collected during LHC Run 2 corresponding to an integrated luminosity of 137.0 fb^{-1}. This is because previous analyses have only been carried out for a luminosity of 35.9 fb^{-1}. As there is a noticeable effect from the higher luminosity as demonstrated by this thesis, it is hoped that there will be much to learn from the upcoming analyses of the full LHC Run 2 data set.
The second major event is the start of a new LHC run in 2022, the LHC RUN 3, which will be performed with $\sqrt{s} = 14$ TeV and an even higher luminosity. It is hoped that this will reveal further possible insights into physics, which will probably also open up new possibilities within MUSiC analyses.

9 Acknowledgement

Finally, I would like to thank a few people here. I would like to thank Prof. Dr. Thomas Hebbeker for allowing me to work on this great project and for giving me further insights into the future of physics. I would also like to thank the MUSiC team members Dr. Saranya Ghosh and M.Sc. Lorenzo Vigilante, who served as mentors during this work and were always there to help me with any kind of complications. I would also like to thank Matthias Bovelett and M.Sc. Ronald Oellers who participated in proofreading this thesis. And then I would like to thank four very special people in my life. My parents Eric & Anabela Kaiser, my brother Mikel Kaiser and my girlfriend Evelyne Ibe for all their support in my life. It is through them that I have gained the strength and opportunities that have brought me this far. Therefore a huge "thank you so much for everything you have done for me".

10 Bibliography

1. Duchardt, D. MUSiC: A Model Unspecific Search for New Physics Based on CMS Data at $\sqrt{s} = 8$ TeV. https://web.physik.rwth-aachen.de/~hebbeker/theses/duchardt_phd.pdf (Aug. 2017).
2. CERN. The Standard Model. https://home.cern/science/physics/standard-model.
3. Lieb, J. Development of a Fast Search Algorithm for the MUSiC Framework. *Bachelor thesis. RWTH Aachen University, Sept,* 50. https://web.physik.rwth-aachen.de/~hebbeker/theses/lieb_bachelor.pdf (Sept. 2015).
4. Stroucken, A. *submitter: Sensitivity Studies for the Model Unspecific Search in CMS (MUSiC) at $\sqrt{s} = 13$ TeV* PhD thesis (RWTH Aachen U., Aug. 2016). https://web.physik.rwth-aachen.de/~hebbeker/theses/stroucken_bachelor.pdf.
5. Rehbein, F. Search for sphalerons in the eμ final state at $\sqrt{s} = 13$ TeV with the CMS experiment. https://web.physik.rwth-aachen.de/~hebbeker/theses/rehbein_bachelor_corrected.pdf (Aug. 2018).
6. PBS NOVA, Fermilab, Office of Science, United States Department of Energy, Particle Data Group. https://commons.wikimedia.org/w/index.php?curid=4286964 (Sept. 2019).
7. Brunner, D. Suche nach zusätzlichen Raumdimensionen im Massenspektrum von zwei Elektronen bei $\sqrt{s} = 13$ TeV. https://web.physik.rwth-aachen.de/~hebbeker/theses/brunner_bachelor.pdf (Aug. 2016).
8. Higgs, P. W. Broken Symmetries and the Masses of Gauge Bosons. *Phys. Rev. Lett.* **13,** 508–509. https://link.aps.org/doi/10.1103/PhysRevLett.13.508 (16 Oct. 1964).
9. Englert, F. & Brout, R. Broken Symmetry and the Mass of Gauge Vector Mesons. *Phys. Rev. Lett.* **13,** 321–323. https://link.aps.org/doi/10.1103/PhysRevLett.13.321 (9 Aug. 1964).
10. Guralnik, G. S., Hagen, C. R. & Kibble, T. W. B. Global Conservation Laws and Massless Particles. *Phys. Rev. Lett.* **13,** 585–587. https://link.aps.org/doi/10.1103/PhysRevLett.13.585 (20 Nov. 1964).
11. Aad, G. *et al.* Observation of a new particle in the search for the Standard Model Higgs boson with the ATLAS detector at the LHC. *Physics Letters B* **716,** 1–29. ISSN: 0370-2693. http://dx.doi.org/10.1016/j.physletb.2012.08.020 (Sept. 2012).

12. Chatrchyan, S. *et al.* Observation of a new boson at a mass of 125 GeV with the CMS experiment at the LHC. *Physics Letters B* **716,** 30–61. ISSN: 0370-2693. http://dx.doi.org/10.1016/j.physletb.2012.08.021 (Sept. 2012).

13. Group, P. D. *et al.* Review of particle physics. *Progress of Theoretical and Experimental Physics* **2020,** 083C01. https://pdg.lbl.gov/2020/download/db2020.pdf (2020).

14. Aad, G. *et al.* Measurements of the Higgs boson production and decay rates and constraints on its couplings from a combined ATLAS and CMS analysis of the LHC pp collision data at $\sqrt{s} = 7$ and 8 TeV. https://link.springer.com/content/pdf/10.1007/JHEP08(2016)045.pdf (2016).

15. Pieta, H. MUSiC. A model unspecific search in CMS based on 2010 LHC data. https://web.physik.rwth-aachen.de/~hebbeker/theses/pieta_phd.pdf (June 2012).

16. Parida, M. K. & Samantaray, R. Unification predictions with or without supersymmetry. *The European Physical Journal Special Topics* **229,** 3243–3262. ISSN: 1951-6401. http://dx.doi.org/10.1140/epjst/e2020-000024-x (Dec. 2020).

17. Schmaltz, M. & Tucker-Smith, D. Little Higgs review. *Ann. Rev. Nucl. Part. Sci.* **55,** 229–270. arXiv: hep-ph/0502182. https://inspirehep.net/literature/677093 (2005).

18. Appelquist, T., Cheng, H.-C. & Dobrescu, B. A. Bounds on universal extra dimensions. *Phys. Rev. D* **64,** 035002. arXiv: hep-ph/0012100. https://inspirehep.net/literature/538212 (2001).

19. Mohapatra, R. N. & Pati, J. C. Left-Right Gauge Symmetry and an Isoconjugate Model of CP Violation. *Phys. Rev. D* **11,** 566–571. https://inspirehep.net/literature/89314 (1975).

20. Altarelli, G., Mele, B. & Ruiz-Altaba, M. Searching for new heavy vector bosons in $p\bar{p}$ colliders. *Zeitschrift für Physik C Particles and Fields* **45,** 109–121. https://link.springer.com/article/10.1007/BF01556677 (Mar. 1989).

21. Duffty, D. & Sullivan, Z. Model independent reach for W' bosons at the LHC. *Physical Review D* **86.** ISSN: 1550-2368. http://dx.doi.org/10.1103/PhysRevD.86.075018 (Oct. 2012).

22. Lincoln, D. The Z boson's heavy cousin. https://news.fnal.gov/2013/02/the-z-boson-s-heavy-cousin/ (Feb. 2013).

23. Sirunyan, A. M. *et al.* Search for high-mass resonances in final states with a lepton and missing transverse momentum at $\sqrt{s} = 13$ TeV. *Journal of High Energy Physics* **2018,** 1–43. https://arxiv.org/abs/1803.11133 (June 2018).

24. Note, A. P. Prospects for searches for heavy Z and W bosons in fermionic final states with the ATLAS experiment at the HL-LHC. https://cds.cern.ch/record/2650549/files/ATL-PHYS-PUB-2018-044.pdf?version=2 (2018).

25. Zuo, Y.-B., Yue, C.-X., Yang, W., Hao, Y.-N. & Zhang, W.-R. New gauge boson W' and radiative leptonic decays of charged B and D mesons. *The European Physical Journal C* **78,** 571. https://link.springer.com/content/pdf/10.1140/epjc/s10052-018-6044-1.pdf (2018).

26. Klinkhamer, F. *Sphalerons in the Standard Model* 2016. https://www.rug.nl/research/vsi/events/groenewold/klinkhamer.pdf.

27. Ho, D. L.-J. & Rajantie, A. Electroweak sphaleron in a strong magnetic field. *Physical Review D* **102.** ISSN: 2470-0029. http://dx.doi.org/10.1103/PhysRevD.102.053002 (Sept. 2020).

28. Satco, D. Search for Sphalerons in Proton-Proton Collisions. https://cds.cern.ch/record/2278326 (Aug. 2017).

29. Khoze, V. V. & Milne, D. L. *Suppression of Electroweak Instanton Processes in High-energy Collisions* 2020. arXiv: 2011.07167 [hep-ph]. https://arxiv.org/pdf/2011.07167.

30. Tye, S.-H. H. & Wong, S. S. C. The Chern–Simons number as a dynamical variable. *Annals of Mathematical Sciences and Applications* **1,** 123–147. ISSN: 2380-2898. http://dx.doi.org/10.4310/amsa.2016.v1.n1.a3 (2016).

31. Sirunyan, A. M. *et al.* Search for black holes and sphalerons in high-multiplicity final states in proton-proton collisions at $\sqrt{s} = 13$ TeV. *Journal of High Energy Physics* **2018.** ISSN: 1029-8479. http://dx.doi.org/10.1007/JHEP11(2018)042 (Nov. 2018).

32. Mouche, P. Overall view of the LHC. Vue d'ensemble du LHC. General Photo. https://cds.cern.ch/record/1708847 (June 2014).

33. Lefèvre, C. *The CERN accelerator complex. Complexe des accélérateurs du CERN* Dec. 2008. https://cds.cern.ch/record/1260465.

34. CERN. Facts and figures about the LHC. https://home.cern/resources/faqs/facts-and-figures-about-lhc.

35. AFP. A view of Compact Muon Solenoid (CMS) Cavern at the European Organization for Nuclear Research (CERN). Photo by Richard Juilliart. https://sciencesprings.wordpress.com/2016/09/06/from-sixth-tone-nobel-winner-says-china-should-not-build-particle-collider/ (Feb. 2015).

36. Collaboration, T. C. The CMS experiment at the CERN LHC. *Journal of Instrumentation* **3,** S08004–S08004. https://doi.org/10.1088/1748-0221/3/08/s08004 (Aug. 2008).

37. Collaboration, C. *MUSiC: A model unspecific search for new physics in proton-proton collisions at $\sqrt{s} = 13$ TeV* 2020. arXiv: 2010.02984 [hep-ex]. https://arxiv.org/abs/2010.02984.

38. Sakuma, T. & McCauley, T. Detector and Event Visualization with SketchUp at the CMS Experiment. *Journal of Physics: Conference Series* **513,** 022032. https://doi.org/10.1088/1742-6596/513/2/022032 (June 2014).

39. Sirunyan, A. *et al.* Performance of the CMS muon detector and muon reconstruction with proton-proton collisions at $\sqrt{s} = 13$ TeV. *Journal of Instrumentation* **13,** P06015–P06015. ISSN: 1748-0221. http://dx.doi.org/10.1088/1748-0221/13/06/P06015 (June 2018).

40. Kleine-Limberg, F. Inorganic scintillator calorimeters: CMS. http://www.kip.uni-heidelberg.de/atlas/seminars/WS2009_JC/CMS.pdf (Nov. 2009).

41. Bayer, A. E. & Seljak, U. The look-elsewhere effect from a unified Bayesian and frequentist perspective. *Journal of Cosmology and Astroparticle Physics* **2020,** 009–009. ISSN: 1475-7516. http://dx.doi.org/10.1088/1475-7516/2020/10/009 (Oct. 2020).

42. Butterworth, J. *et al.* PDF4LHC recommendations for LHC Run II. *Journal of Physics G: Nuclear and Particle Physics* **43,** 023001. ISSN: 1361-6471. http://dx.doi.org/10.1088/0954-3899/43/2/023001 (Jan. 2016).

43. Bravo, C. & Hauser, J. BaryoGEN, a Monte Carlo generator for sphaleron-like transitions in proton-proton collisions. *Journal of High Energy Physics* **2018.** ISSN: 1029-8479. http://dx.doi.org/10.1007/JHEP11(2018)041 (Nov. 2018).

44. Lai, H.-L. *et al.* New parton distributions for collider physics. *Phys. Rev. D* **82,** 074024. https://link.aps.org/doi/10.1103/PhysRevD.82.074024 (7 Oct. 2010).

45. Ellis, J. & Sakurai, K. Search for sphalerons in proton-proton collisions. *Journal of High Energy Physics* **2016,** 86. https://link.springer.com/article/10.1007/JHEP04(2016)086 (2016).

11 Appendix

11.1 Further figures of the W′ study

11.1.1 $M_{W'} = 2$ TeV

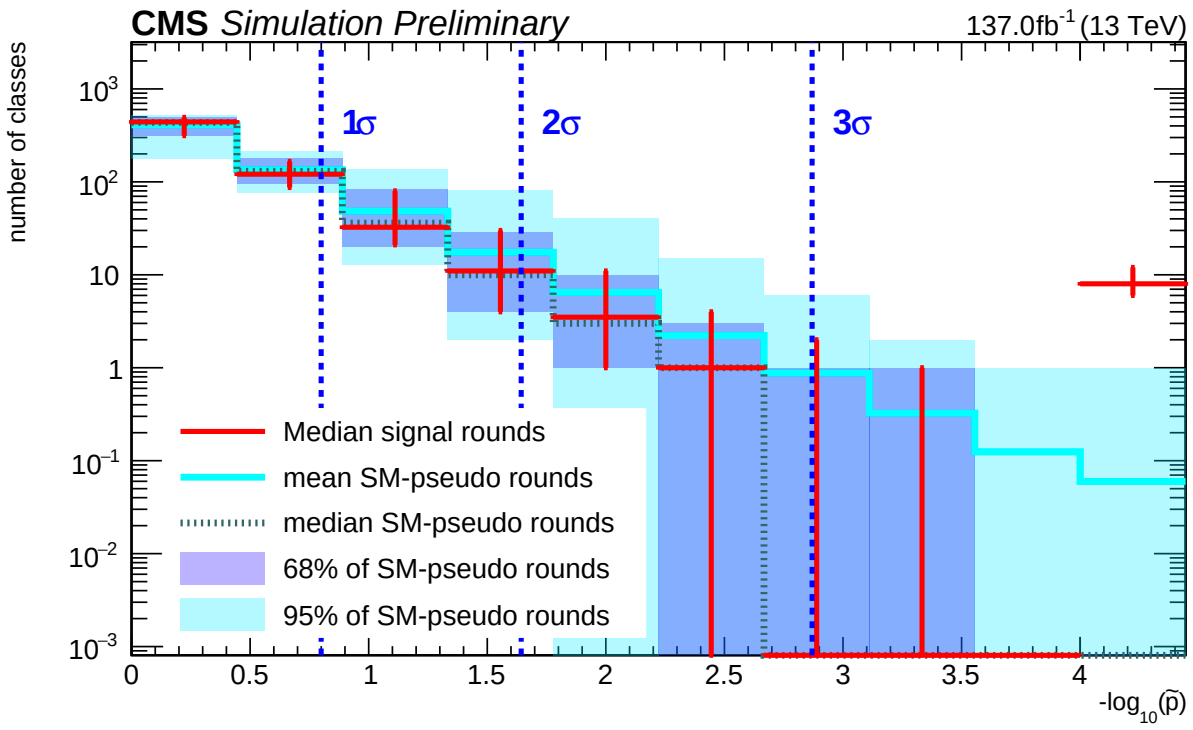

Fig. 11.1: Histogram of $\tilde{p}$-values for the kinematic distribution M_{inv} for $M_{W'} = 2$ TeV in 2021.

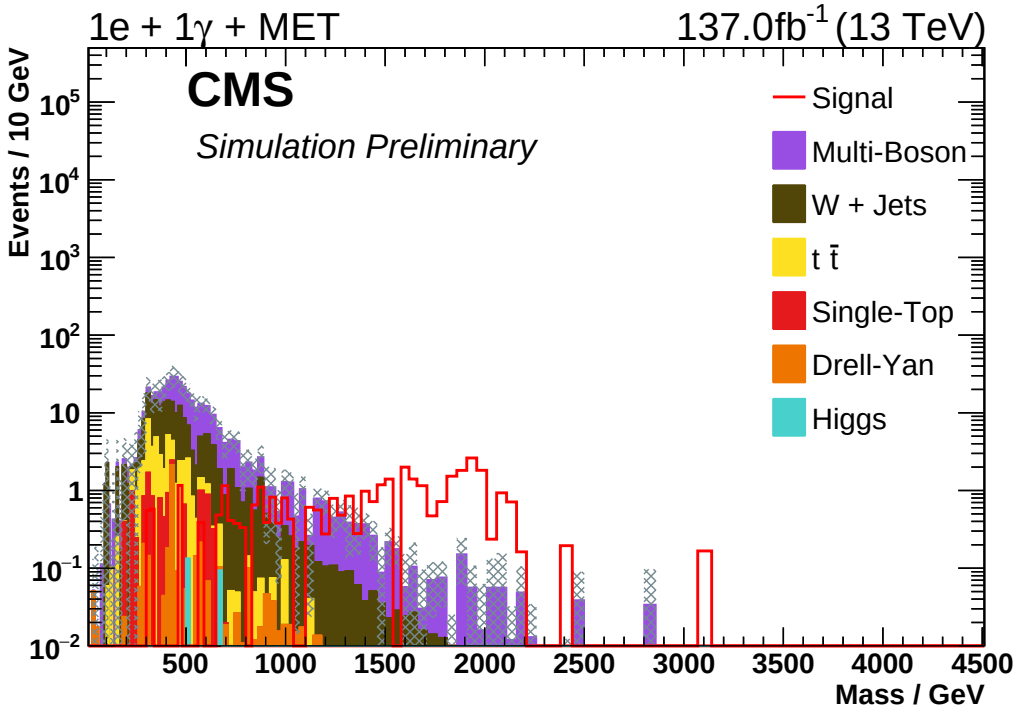

Fig. 11.2: Distribution of the transverse mass of a hypothetical W′ ($M_{W'}$ = 2 TeV) for the $1e$+1γ+MET exclusive class.

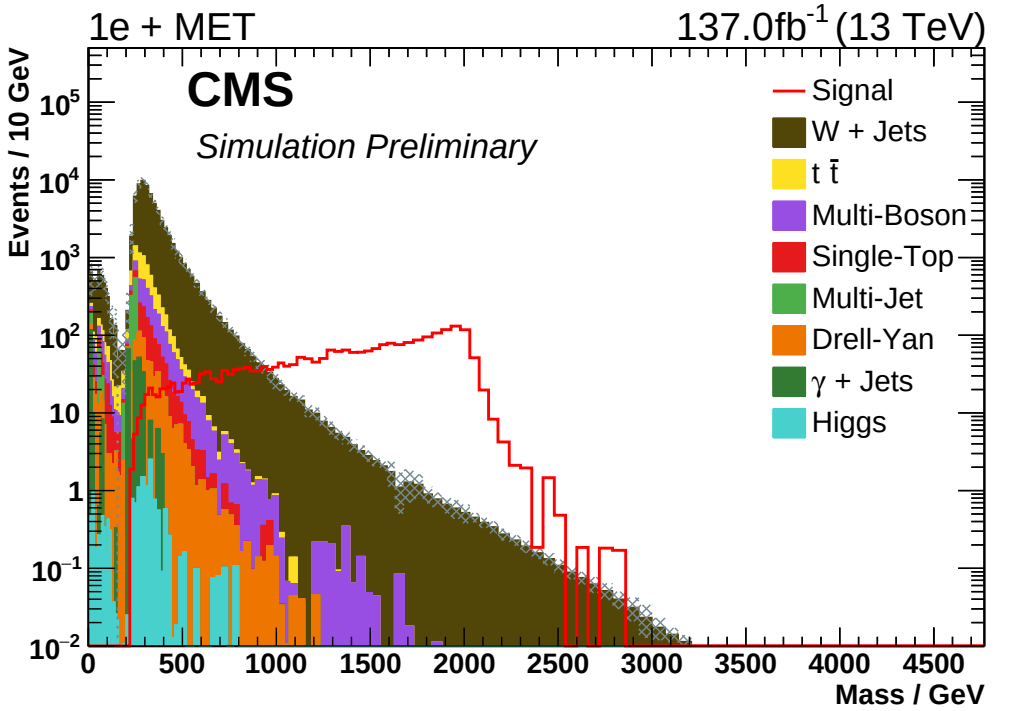

Fig. 11.3: Distribution of the transverse mass of a hypothetical W′ ($M_{W'}$ = 2 TeV) for the $1e$+MET exclusive class.

11.1.2 $M_{W'} = 3$ TeV

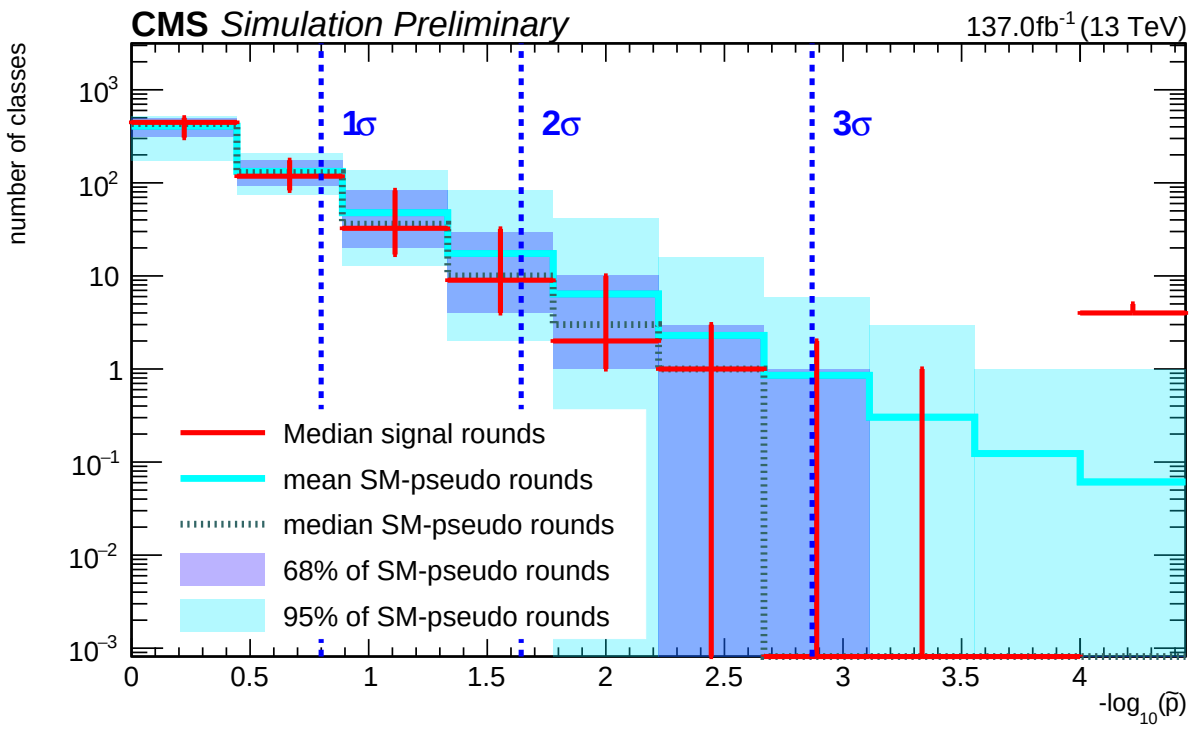

Fig. 11.4: Histogram of $\tilde{p}$-values for the kinematic distribution M_{inv} for $M_{W'} = 3$ TeV in 2021.

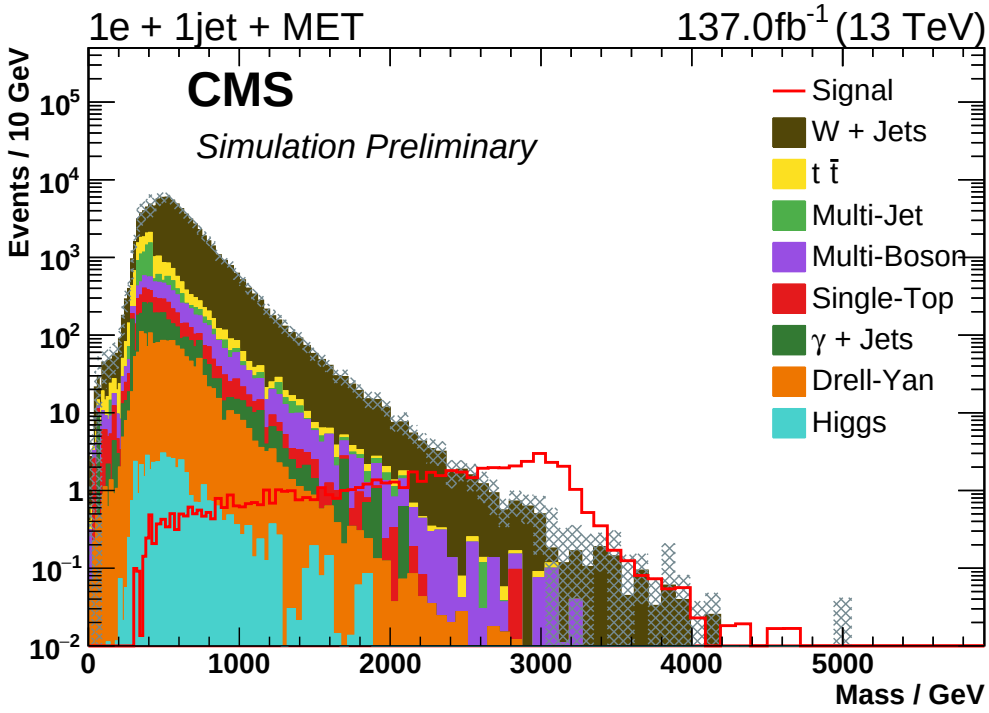

Fig. 11.5: Distribution of the transverse mass of a hypothetical W′ ($M_{W'} = 3$ TeV) for the $1e$+1Jet+MET exclusive class.

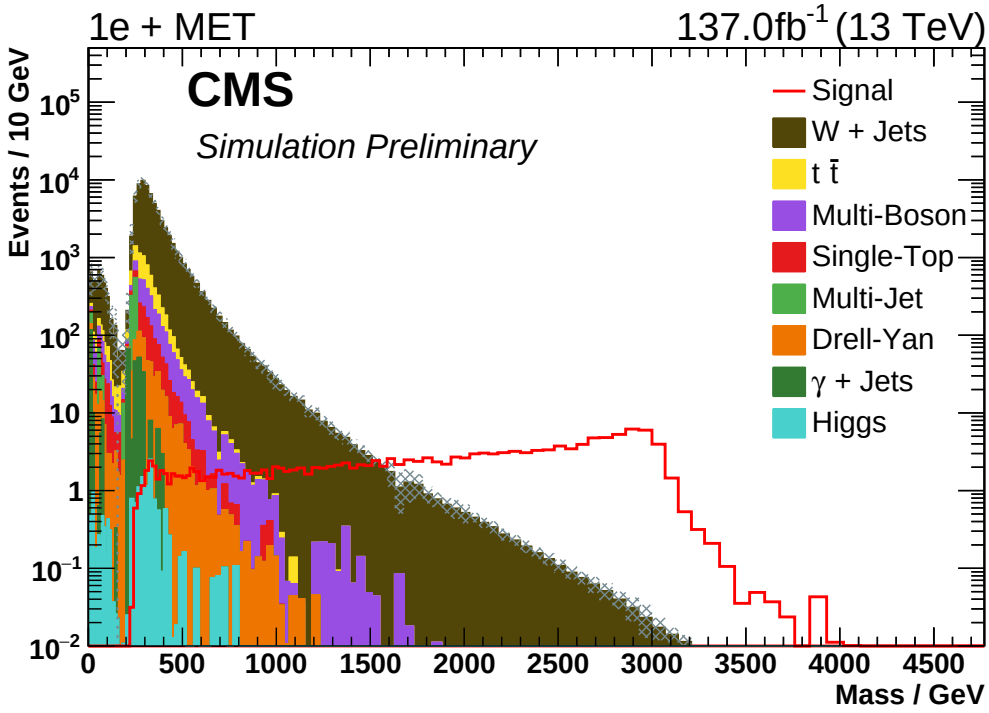

Fig. 11.6: Distribution of the transverse mass of a hypothetical W′ ($M_{W'} = 3$ TeV) for the $1e$+MET exclusive class.

11.1.3 $M_{W'}$ = 4 TeV

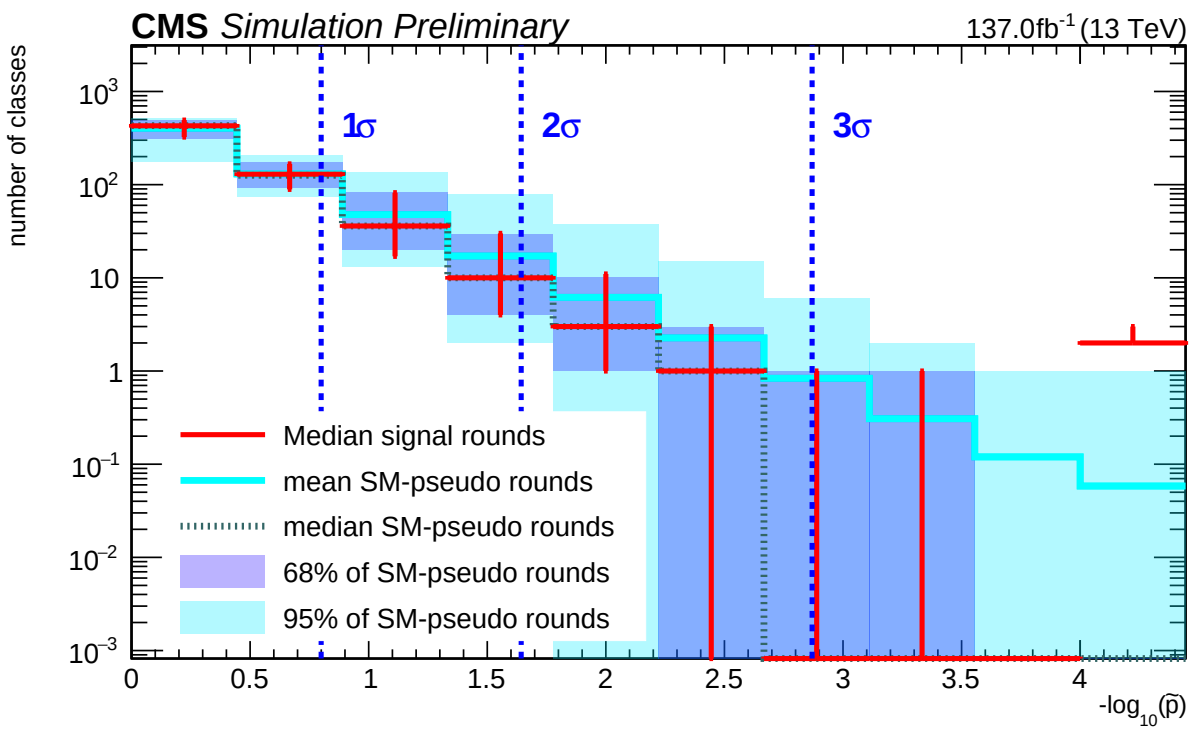

Fig. 11.7: Histogram of $\tilde{p}$-values for the kinematic distribution M_{inv} for $M_{W'} = 4$ TeV in 2021.

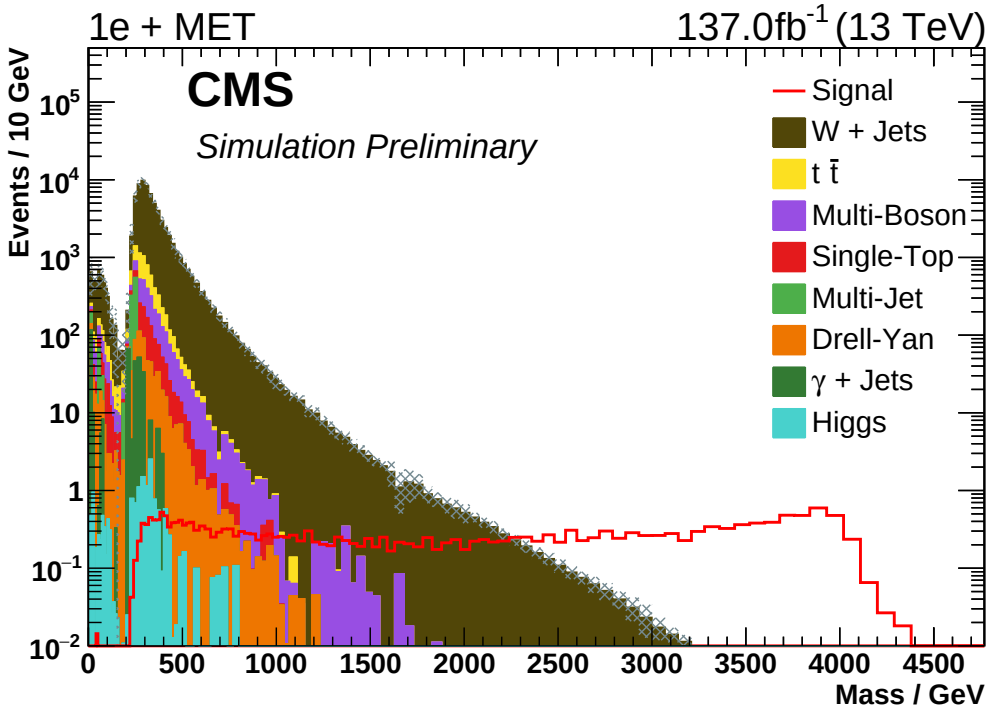

Fig. 11.8: Distribution of the transverse mass of a hypothetical W′ ($M_{W'} = 4$ TeV) for the $1e$+MET exclusive class.

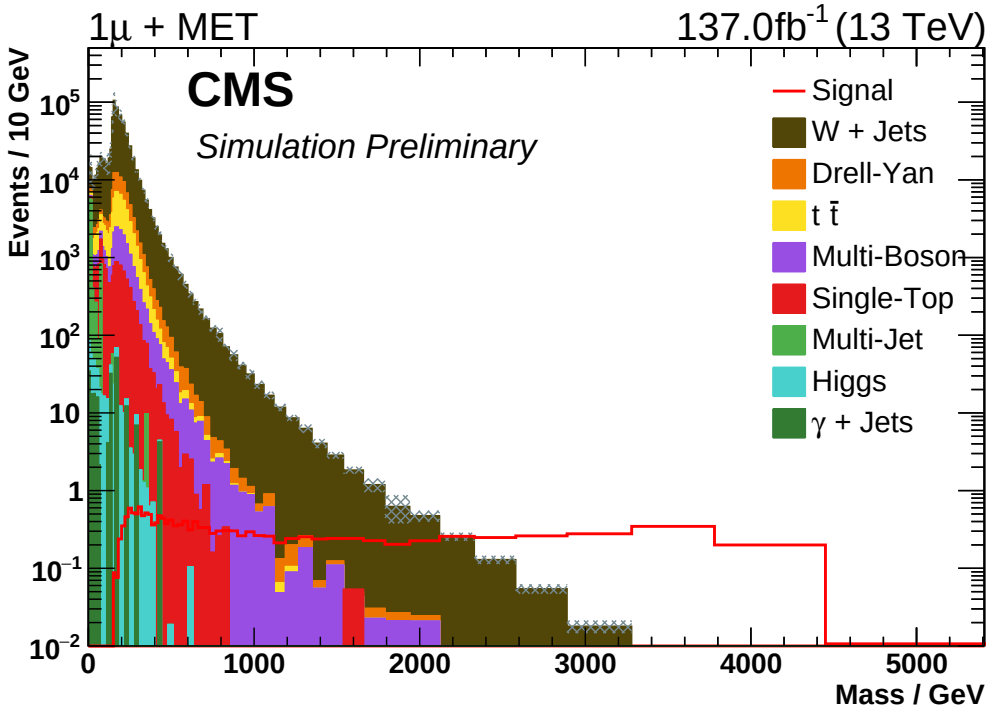

Fig. 11.9: Distribution of the transverse mass of a hypothetical W′ ($M_{W'} = 4$ TeV) for the 1μ+MET exclusive class.

11.1.4 $M_{W'} = 5$ TeV

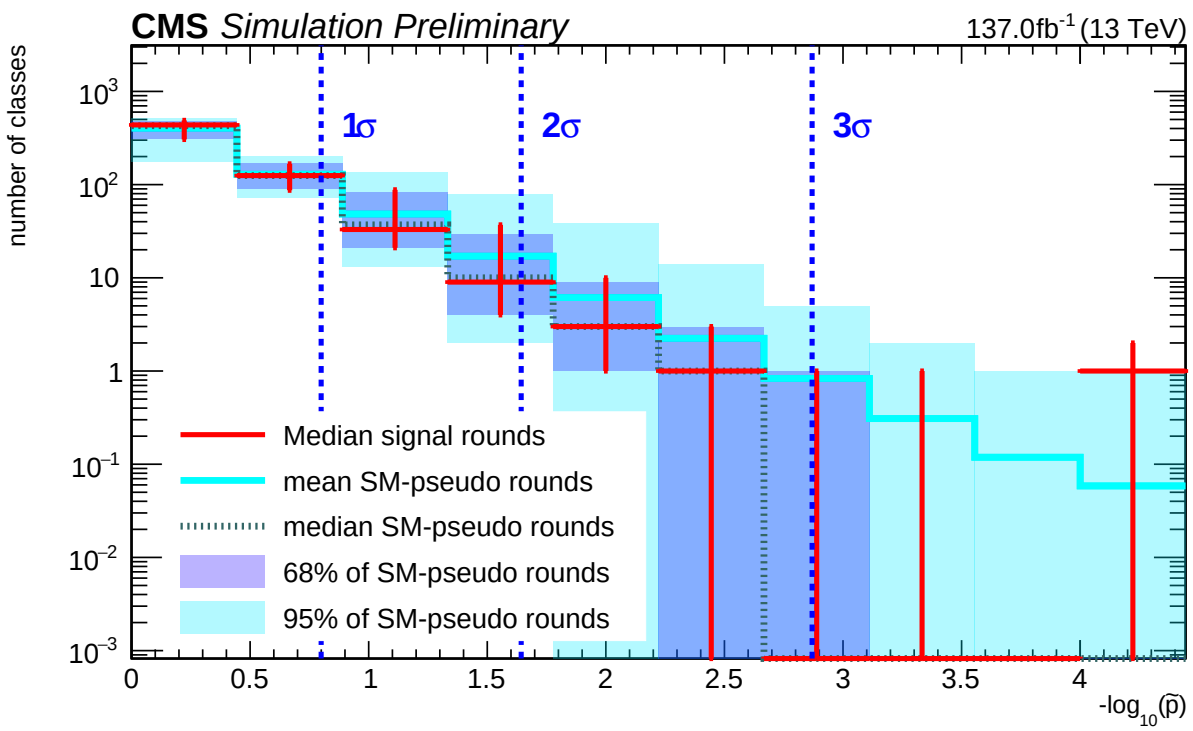

Fig. 11.10: Histogram of $\tilde{p}$-values for the kinematic distribution M_{inv} for $M_{W'} = 5$ TeV in 2021.

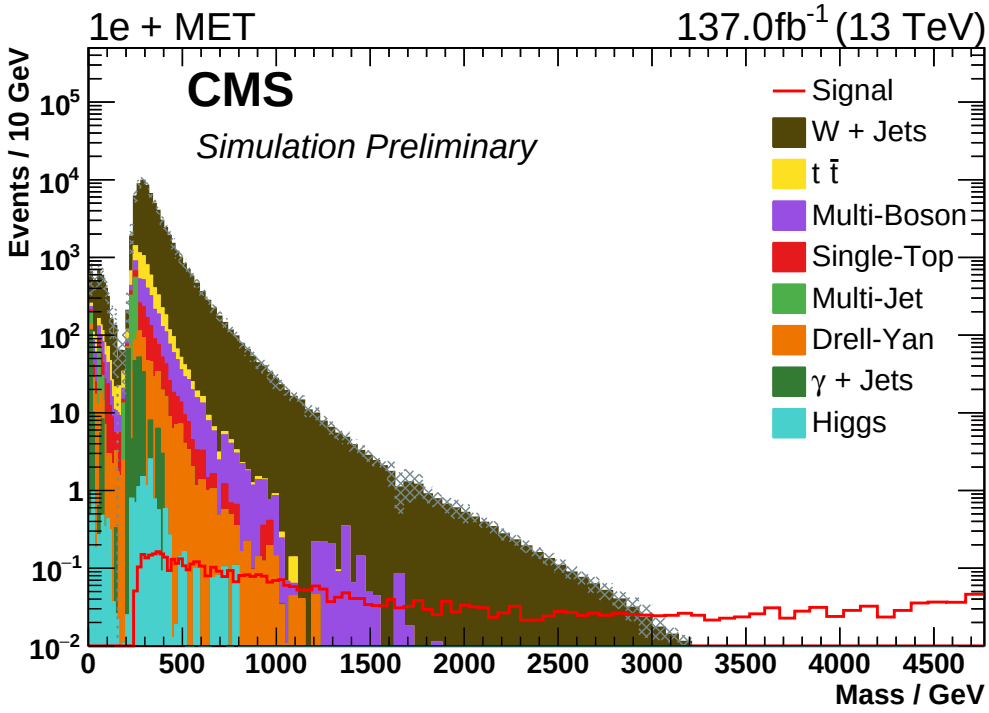

Fig. 11.11: Distribution of the transverse mass of a hypothetical W′ ($M_{W'} = 5$ TeV) for the $1e$+MET exclusive class.

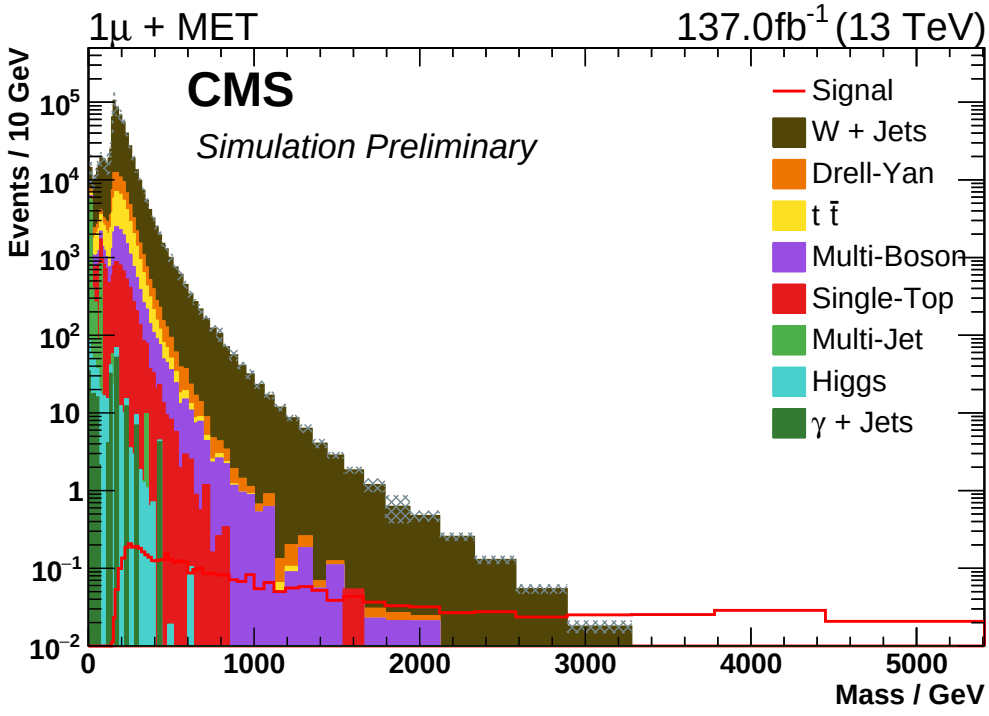

Fig. 11.12: Distribution of the transverse mass of a hypothetical W′ ($M_{W'} = 5$ TeV) for the 1μ+MET exclusive class.

11.2 Further figures of the sphaleron study

11.2.1 PEF = 0.01

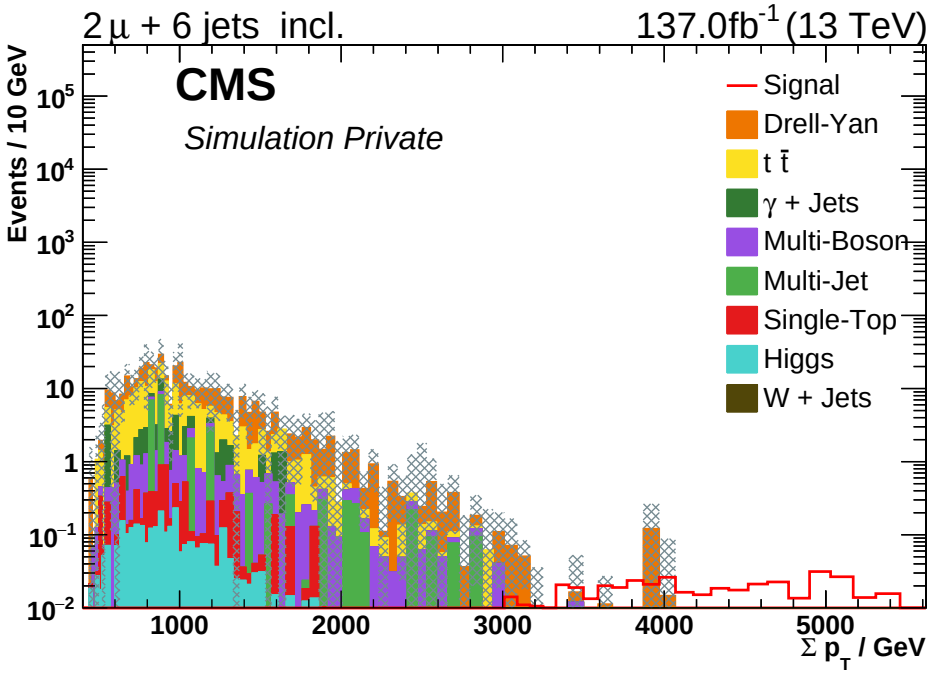

Fig. 11.13: Distributions of S_T of a hypothetical Sphaleron with PEF = 0.01 for the 2μ+6Jet+X inclusive class.

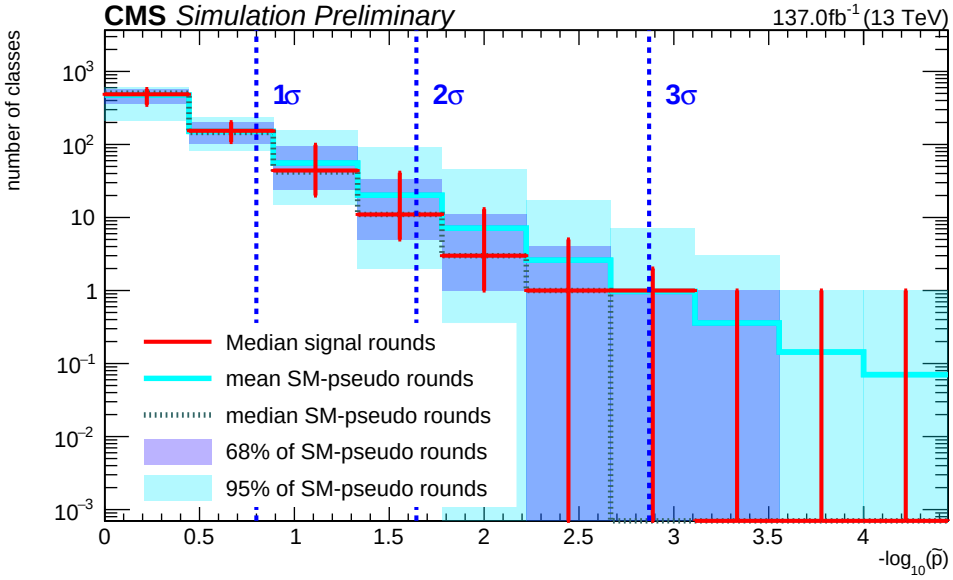

Fig. 11.14: Histogram of $\tilde{p}$-values for the kinematic distribution S_T in the jet-inclusive class for PEF = 0.01 of the Sphaleron study in 2021.

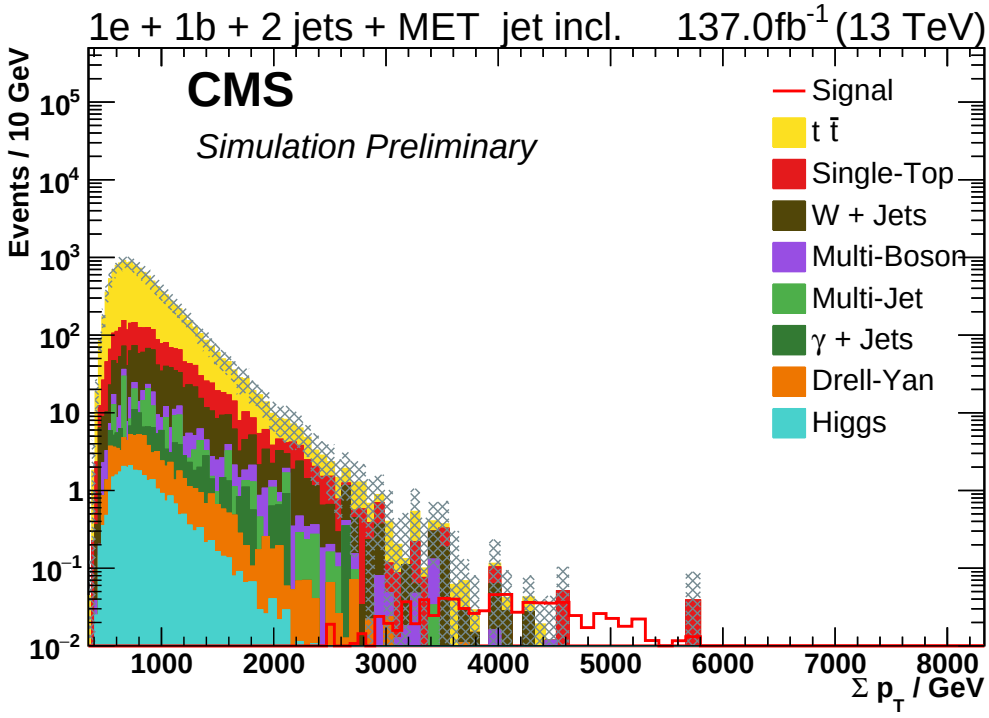

Fig. 11.15: Distributions of S_T of a hypothetical Sphaleron with PEF = 0.01 for the $1e$+1bJet+2Jet+MET+NJet jet-inclusive class.

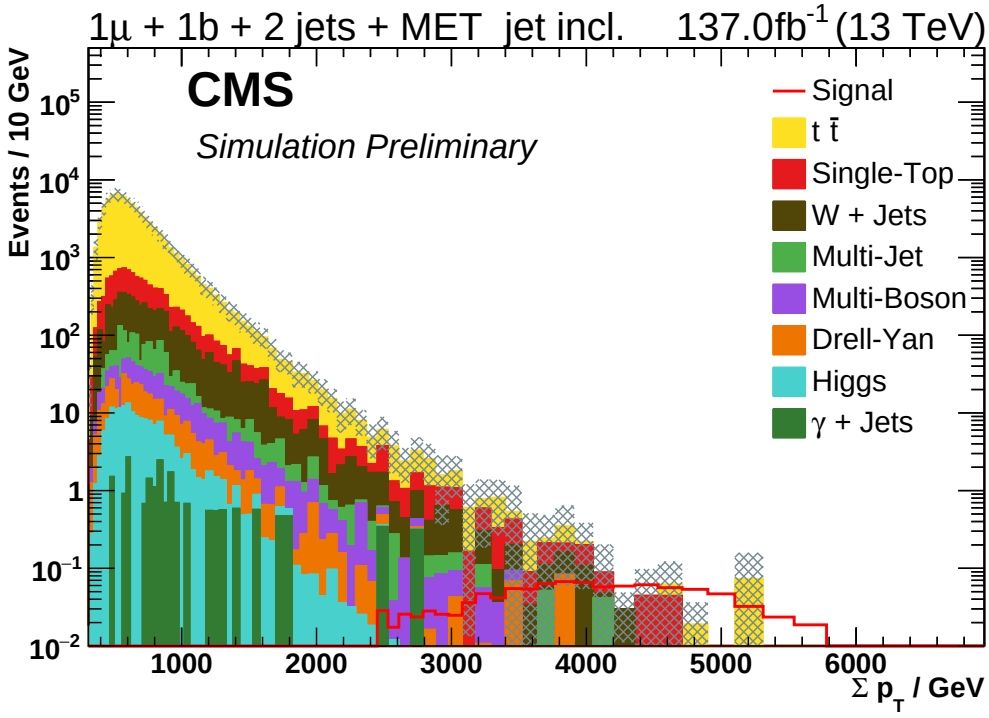

Fig. 11.16: Distributions of S_T of a hypothetical Sphaleron with PEF = 0.01 for the 1μ+1bJet+2Jet+MET+NJet jet-inclusive class.

11.2.2 PEF = 0.02

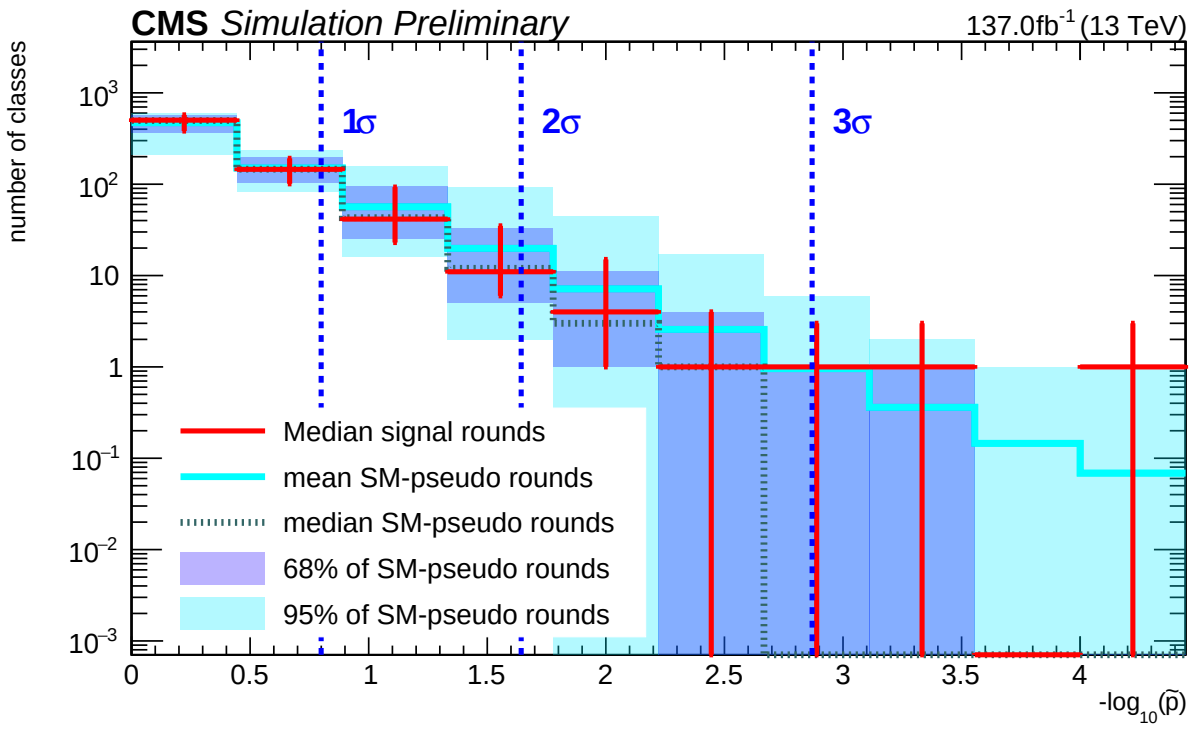

Fig. 11.17: Histogram of $\tilde{p}$-values for the kinematic distribution S_T in the jet-inclusive class for PEF = 0.02 of the Sphaleron study in 2021.

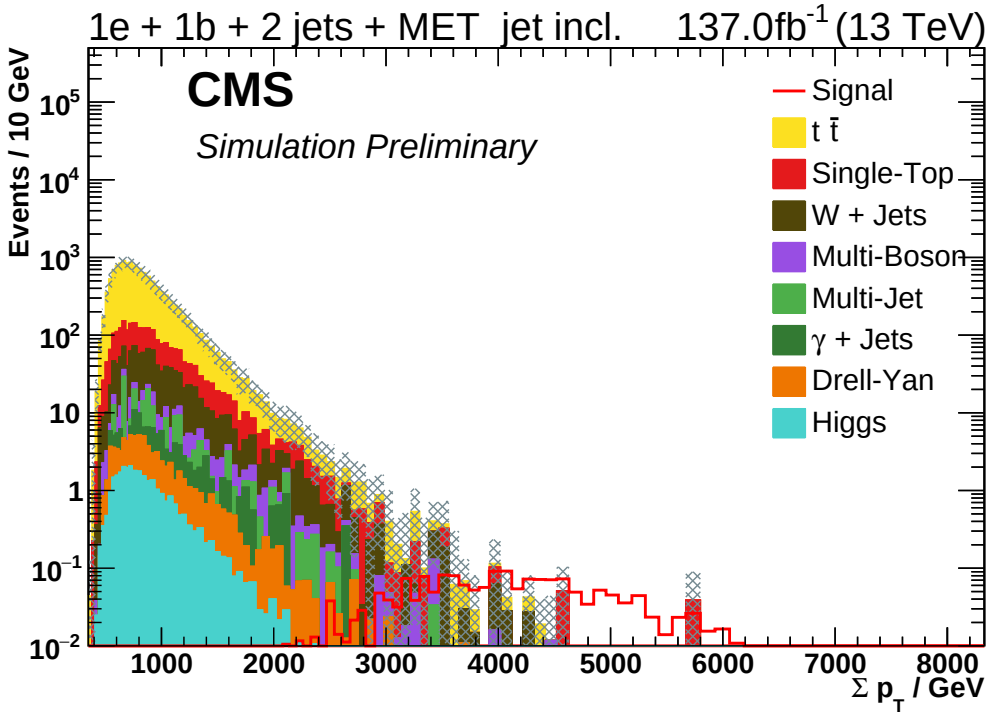

Fig. 11.18: Distributions of S_T of a hypothetical Sphaleron with PEF = 0.02 for the $1e$+1bJet+2Jet+MET+NJet jet-inclusive class.

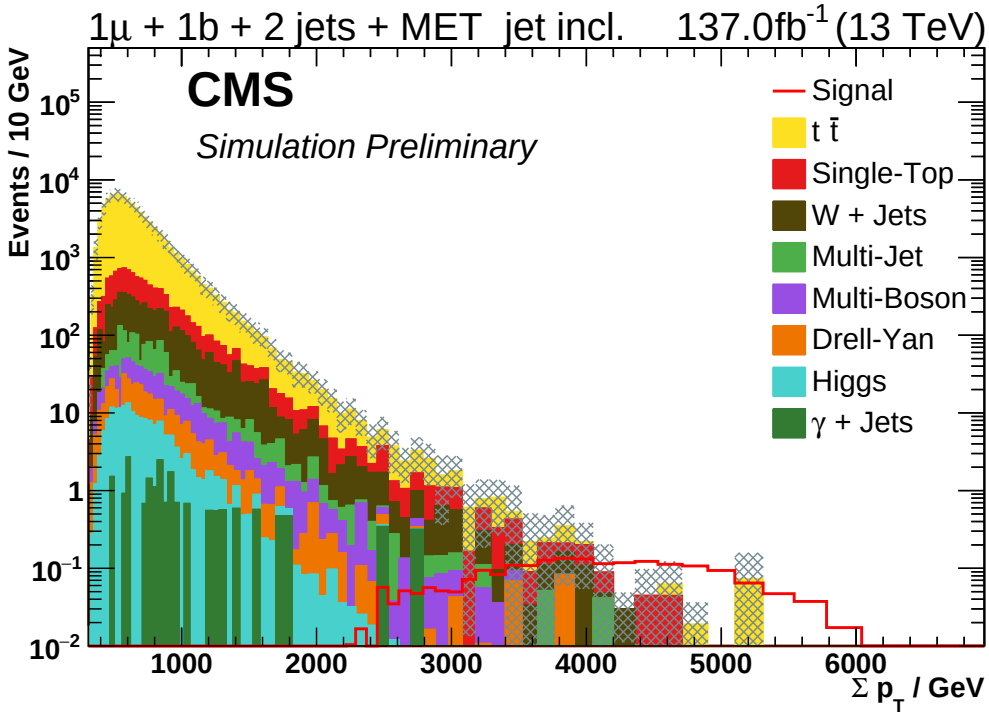

Fig. 11.19: Distributions of S_T of a hypothetical Sphaleron with PEF = 0.02 for the 1μ+1bJet+2Jet+MET+NJet jet-inclusive class.

11.2.3 PEF = 0.025

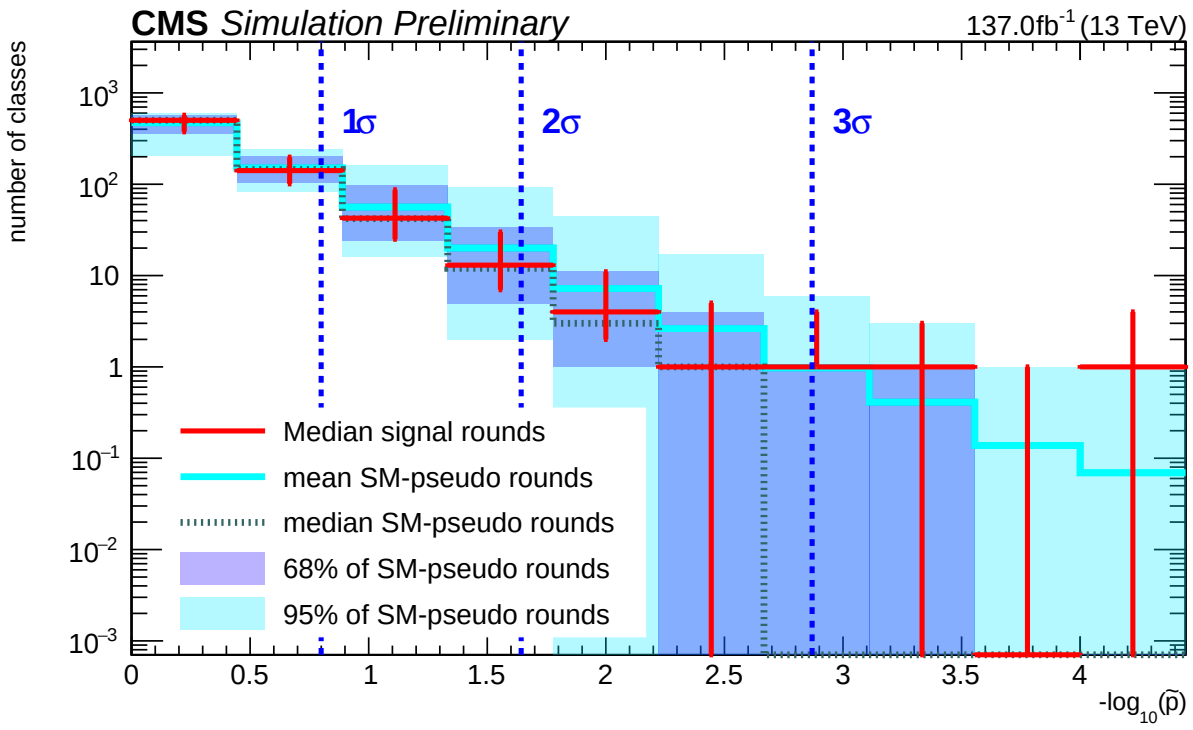

Fig. 11.20: Histogram of $\tilde{p}$-values for the kinematic distribution S_T in the jet-inclusive class for PEF = 0.025 of the Sphaleron study in 2021.

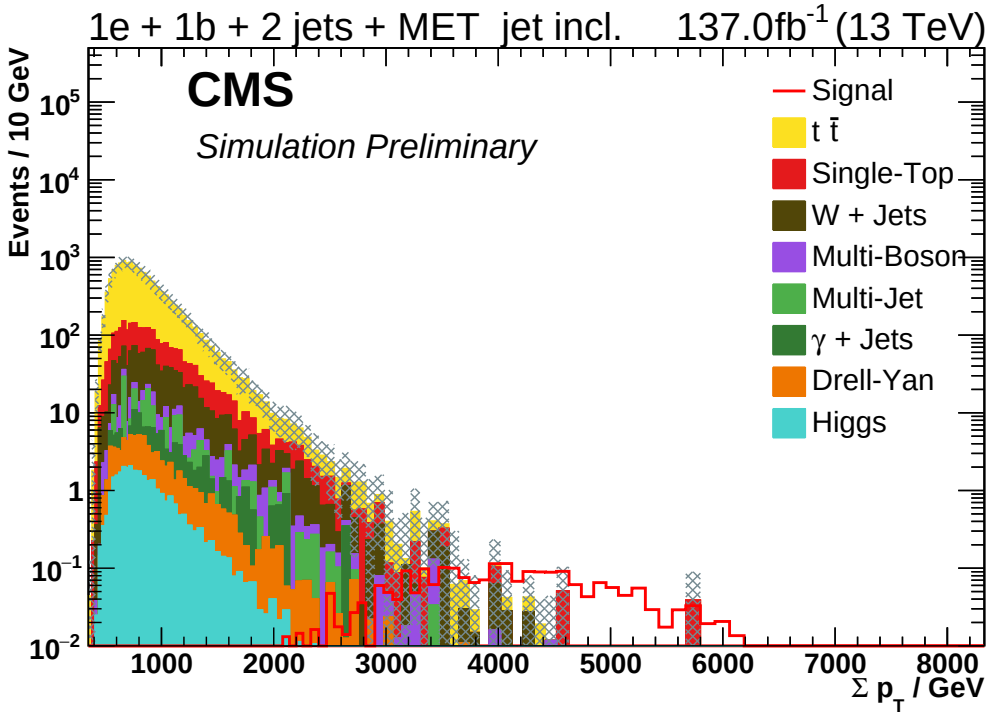

Fig. 11.21: Distributions of S_T of a hypothetical Sphaleron with PEF = 0.025 for the $1e$+1bJet+2Jet+MET+NJet jet-inclusive class.

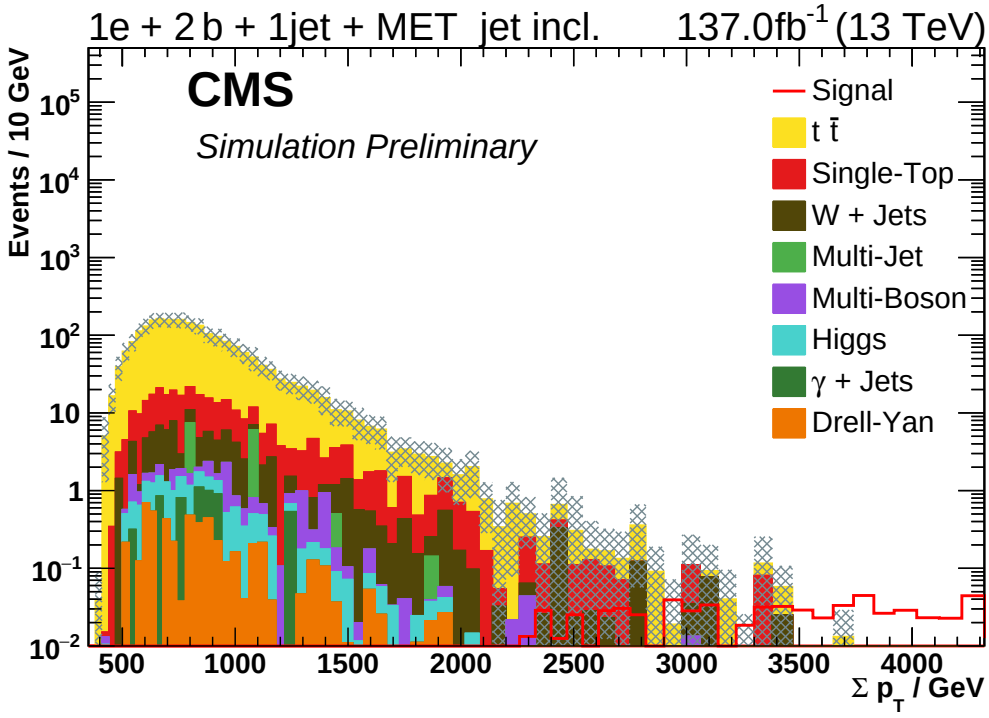

Fig. 11.22: Distributions of S_T of a hypothetical Sphaleron with PEF = 0.025 for the $1e$+2bJet+1Jet+MET+NJet jet-inclusive class.

11.2.4 PEF = 0.05

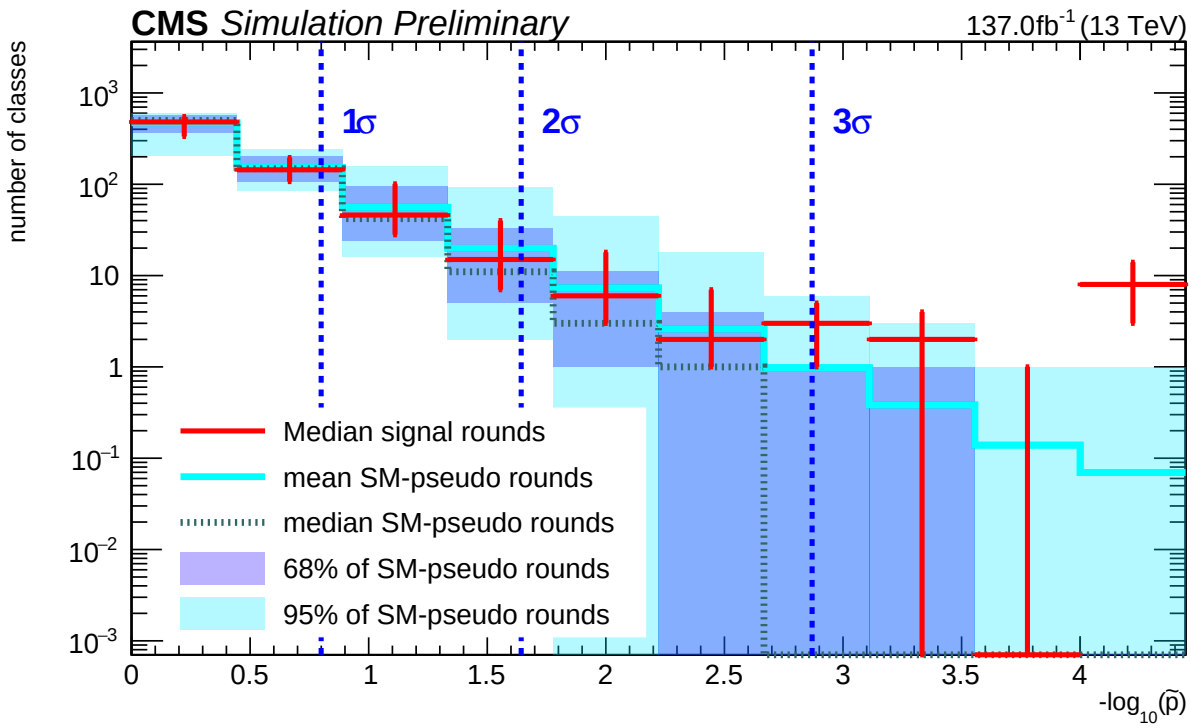

Fig. 11.23: Histogram of $\tilde{p}$-values for the kinematic distribution S_T in the jet-inclusive class for PEF = 0.05 of the Sphaleron study in 2021.

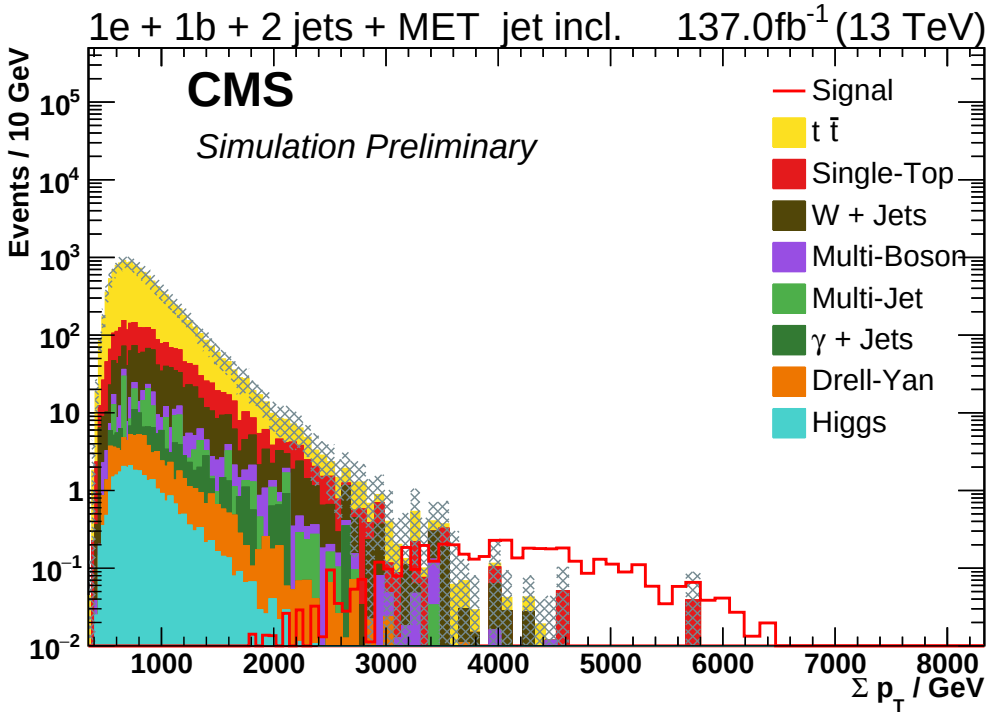

Fig. 11.24: Distributions of S_T of a hypothetical Sphaleron with PEF = 0.05 for the $1e$+1bJet+2Jet+MET+NJet jet-inclusive class.

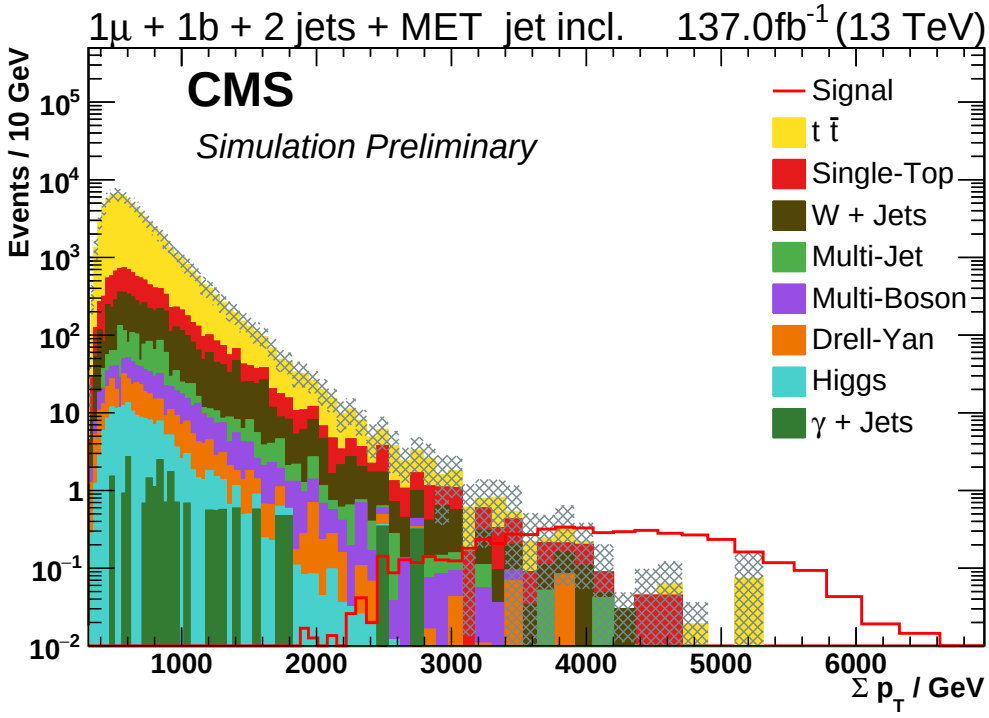

Fig. 11.25: Distributions of S_T of a hypothetical Sphaleron with PEF = 0.05 for the 1μ+1bJet+2Jet+MET+NJet jet-inclusive class.